J. Fluid Mech. (2020), *vol*. 900, A25. © The Author(s), 2020.
Published by Cambridge University Press
doi:10.1017/jfm.2020.467

Variation of leading-edge suction during stall for unsteady aerofoil motions

Shreyas Narsipur[1],†, **Pranav Hosangadi**[1], **Ashok Gopalarathnam**[1] and **Jack R. Edwards**[1]

[1]Department of Mechanical and Aerospace Engineering, North Carolina State University, Raleigh, NC 27695, USA

(Received 24 September 2019; revised 6 June 2020; accepted 6 June 2020)

The suction force at the leading edge of a round-nosed aerofoil is an important indicator of the state of the flow over the leading edge and, often, the entire aerofoil. The leading-edge suction parameter (LESP) is a non-dimensional version of this force. In recent works, the LESP was calculated with good accuracy for attached flows at low Reynolds numbers (10 000–100 000) from unsteady aerofoil theory. In contrast to this 'inviscid' LESP, results from viscous computations and experiments are used here to calculate the 'viscous' LESP on aerofoils undergoing pitching motions at low subsonic speeds. The LESP formulation is also updated to account for the net velocity of the aerofoil. Spanning multiple aerofoils, Reynolds numbers and kinematics, the cases include motions in which dynamic stall occurs with or without leading-edge vortex (LEV) formation. Inflections in the surface pressure and skin-friction distributions near the leading edge are shown to be reliable indicators of LEV initiation. Critical LESP, which is the LESP value at LEV initiation, was found to be nearly independent of pivot location, weakly dependent on pitch rate and strongly dependent on Reynolds number. The viscous LESP was seen to drop to near-zero values when the flow is separated at the leading edge, irrespective of LEV formation. This behaviour was shown to correlate well with the loss of streamline curvature at the leading edge due to flow separation. These findings serve to improve our understanding and extend the applicability of the leading-edge suction behaviour gained from earlier works.

Key words: boundary layer separation, vortex dynamics, vortex shedding

1. Introduction

It has been known for several decades that the onset of reversed flow at the leading edge of an unsteady aerofoil and the subsequent formation of a leading-edge vortex (LEV) are governed by criticality of flow parameters at the leading edge (Evans & Mort 1959; Beddoes 1978; Ekaterinaris & Platzer 1998; Jones & Platzer 1998). A flow parameter of particular interest is the leading-edge suction force, a non-dimensional version of which is termed the leading-edge suction parameter (LESP) (Ramesh *et al.* 2014). For low-order modelling, the instantaneous value of the LESP is calculated from unsteady aerofoil theory (Ramesh *et al.* 2014). This 'inviscid' LESP, however, is valid only for attached-flow conditions. Here we calculate a 'viscous' version of the LESP by surface

† Email address for correspondence: shreya@ncsu.edu

pressure integration of experimental and viscous-computational results to understand the effects of flow separation on the variation of leading-edge suction. We present a correction factor that updates the formulation of the LESP using the magnitude of the instantaneous net velocity of the aerofoil. We focus on events before, during and after flow separation from the leading edge, both in cases with LEV formation and in cases in which there is no LEV formation. We draw on the flow field results to provide explanations for these trends. By studying a large set of computational results from unsteady Reynolds-averaged Navier–Stokes (RANS) simulations of pitching aerofoils, we present the effects of Reynolds number, pitch rate and pivot location on the criticality of the LESP. The improved understanding resulting from this work is helpful in extending the range of Reynolds numbers and pitch rates over which the LESP criterion and low-order modelling of Ramesh *et al.* (2014) are applicable.

The relevant applications for LEV-dominated unsteady aerodynamics span a wide range that include, but are not limited to, dynamic stall in helicopters and wind turbines (Huyer, Simms & Robinson 1996; Corke & Thomas 2015), bio-inspired flight (Ellington *et al.* 1996), micro air vehicle design (MAV) (Ellington 1999), LEVs in delta wings (Gursul 2005) and flow-energy harvesting devices (Young, Lai & Platzer 2014). While theoretical work in unsteady aerodynamics, primarily by Wagner (1925) and Theodorsen (1935), dates back to the 1920s and 1930s, the late 1960s saw a renewed interest in unsteady fluid flows due to the dynamic stall problem in helicopters (Crimi 1973). Although analytical studies by Carta (1967*a*,*b*) and Ericsson & Reding (1971) helped us understand and predict dynamic stall, the methods were restricted to low pitch-rate motions and the availability of static experimental data. Extensive experimental studies by McCroskey, Carr & McAlister (1976), McAlister, Carr & McCroskey (1978), Carr, McAlister & McCroskey (1977), and McAlister & Carr (1978) provided major leaps in understanding and predicting dynamic stall. McCroskey (1981, 1982) characterized the phenomenon of dynamic stall by a delay in the onset of flow separation and the shedding of concentrated vorticity, popularly known as dynamic-stall vortex or LEV, from the leading edge of the aerofoil. McCroskey *et al.*'*s* three-part review of experimental studies of dynamic stall showed that while pitch rate and aerofoil shape, specifically the leading-edge profile, had major effects on the aerodynamic loads and strength of the LEV, the Reynolds number effects were small (McCroskey *et al.* 1982; McAlister *et al.* 1982; Carr *et al.* 1982).

Improvements in supercomputing capabilities allowed for various aspects of dynamic stall to be extensively studied using computational methods (Visbal & Shang 1989; Choudhuri, Knight & Visbal 1994; Choudhuri & Knight 1996; Wernert *et al.* 1996; Akbari & Price 2003; Hill, Shaw & Qin 2004; Spentzos *et al.* 2004; Geissler & Haselmeyer 2006; Sharma & Visbal 2019; Visbal & Garmann 2019). Recent research interest in insect/bird flight and MAV aerodynamics have pushed the boundaries of unsteady aerodynamics to include time-dependent motions at lower Reynolds numbers and higher pitch rates, and has spurred many computational and experimental studies on the subject (Eldredge, Wang & Ol 2009; Ol *et al.* 2009; Eldredge & Wang 2010; Granlund *et al.* 2010). Meanwhile, based on the findings of experimental and computational studies, theoretical models have been developed and improved for use in rapid design and analysis activities (Gormont 1973; Dat, Tran & Petot 1979; Katz 1981; Leishman & Beddoes 1989; Peters, Karunamoorthy & Cao 1995; Larsen, Nielsen & Krenk 2007; Sheng, Galbraith & Coton 2006, 2008; Yan, Taha & Hajj 2014).

One specific aspect of dynamic stall that has continued to receive some attention is the criticality of leading-edge flow as a causal factor for LEV formation. Based in part on the work by Evans & Mort (1959), which showed that leading-edge separation is directly

related to the strong adverse pressure gradient that follows the suction peak at the leading edge, Beddoes (1978) showed the correspondence between leading-edge separation and the flow velocity at the leading edge. This idea was subsequently incorporated in the Leishman–Beddoes dynamic-stall model (Leishman & Beddoes 1989) for modelling LEV formation. Jones & Platzer (1998) showed that, at the initiation of dynamic stall, indicated by the first occurrence of laminar separation at the leading edge of the aerofoil, the leading-edge flow characteristics (pressure distributions, pressure-gradient distributions, and locations of stagnation and laminar-separation points) are invariant with pitch rate (see also Ekaterinaris & Platzer 1998). However, the value of this critical angle of attack itself was seen to increase with pitch rate, a result that was in qualitative agreement with experimental results of Chandrasekhara, Ahmed & Carr (1993).

More recently, Ramesh *et al.* (2013, 2014) proposed the concept of LESP for predicting LEV formation in unsteady aerofoils at low Reynolds numbers ($Re = 10\,000$–$100\,000$). They showed that, when using unsteady thin-aerofoil theory to predict the aerodynamics in attached-flow conditions, the value of the A_0 term in the Fourier series representation of the bound-vortex-sheet strength can be used as the instantaneous LESP. By comparison with computational fluid dynamic (CFD) solutions and experimental results for LEV initiation on aerofoils undergoing high-rate motions, they further showed that for any given aerofoil and Reynolds numbers, there is a critical value of LESP that always corresponds to LEV initiation, and that this critical value is largely independent of motion kinematics. The benefit of the LESP concept is that, once the critical LESP is obtained through calibration with CFD or experiment for one motion, it can be used to predict initiation of LEV formation for any other motion.

The LESP idea was used to develop a low-order method in which unsteady thin-aerofoil theory was extended to handle intermittent LEV shedding. In this method, named LESP-modulated discrete vortex method (LDVM), unsteady thin-aerofoil theory was augmented with discrete vortex shedding from the leading edge. At any time step, if the instantaneous LESP was predicted to be greater than the predetermined critical value, a discrete vortex was shed so as to bring the LESP back to the critical value. The idea was that a leading edge at some operating condition is able to support a certain limiting amount of suction, and any attempt at increasing the suction beyond that limiting value would result in shedding of vorticity to bring the suction back to the limiting value. This assumption was built upon the observation by Katz (1981) that a leading edge can support some amount of suction even when experiencing separation. With this assumption, in the LDVM code, the LESP value is held constant at the critical value during LEV shedding. Although there was no proof at that time for the constant value of leading-edge suction during LEV shedding, the predictions for the low-Reynolds-number cases from the LDVM code using this implementation agreed well with CFD and experimental results for a variety of pitch and plunge motions (Ramesh *et al.* 2014). Since then, the LESP criterion for modelling LEV formation has been successfully used to study aeroelastic problems (Ramesh, Murua & Gopalarathnam 2015), flow-energy harvesting approaches (Liu *et al.* 2016), machine-learning approaches to modelling separated flows (Eldredge & Jones 2019; Hou, Darakananda & Eldredge 2019), finite-wing LEV formation (Hirato *et al.* 2019) and to also explain some experimental results (Ansell & Mulleners 2020).

More recently, our efforts have been focused on better understanding the behaviour of LESP during LEV shedding. The current work resulted from the recent realization that a ‘viscous’ LESP can be deduced from experiments and viscous computations by integrating the leading-edge pressure distribution. Using this approach, we present here the variation of the viscous LESP during all phases of unsteady motions, including before,

during and after LEV shedding. With the ability to calculate LESP from CFD results, we focus on answering three important questions to advance the LDVM method beyond the work of Ramesh *et al.* (2014). (i) How does critical LESP vary with an increase in Reynolds numbers to helicopter-relevant conditions, and will the critical LESP remain largely motion independent at the higher Reynolds numbers as well? (ii) How does critical LESP vary when the pitch rate is reduced to those similar to helicopter-relevant conditions at which LEV formation is preceded by trailing-edge separation? (iii) How does the instantaneous LESP vary during a motion while LEV shedding is taking place, and does the LESP in fact stay constant at the critical value during LEV shedding?

In this work a large set of computational results from unsteady RANS simulations of pitching aerofoils in incompressible flow, supplemented with a few experimental results from literature, are studied to examine the behaviour of the viscous LESP at various stages during the dynamic-stall process. Effects of aerofoil shape, Reynolds number, pivot location and non-dimensional pitch rate on the LESP behaviour are quantified. The results from these studies are used to seek answers to the questions posed above.

A brief background of the LESP concept is presented in § 2. The next section (§ 3) briefly describes the computational methodology (§ 3.1), presents validation of the CFD against experimental data (§ 3.2), describes a method for extracting the LESP from viscous surface pressure data (§ 3.3) and presents surface signatures for consistent identification of LEV initiation (§ 3.4). Details of the unsteady motions studied in the current work are presented in § 4. In § 5 the variation of the original LESP at LEV initiation is presented for several motions. A large scatter in LESP values is seen for the high-*Re* motions. In § 6 an updated formulation for the LESP is presented using a motion-dependent velocity ratio. This updated LESP is then shown in § 7 to be successful in reducing the scatter in the LESP values for the high-*Re* cases. Motions that do not evince LEV formation are briefly presented in § 8, followed by a discussion of post-leading-edge-separation behaviour in § 9. The final section (§ 10) presents the conclusions drawn from the current research.

2. Background

This section presents background information on the LESP in § 2.1, its connection to LEV initiation in § 2.2 and its behaviour after LEV formation in § 2.3.

2.1. *Leading-edge suction parameter*

Classical thin-aerofoil theory approximates the aerofoil using its camberline with no thickness and, hence, zero leading-edge radius. This assumption requires the flow to turn around the sharp leading edge, giving rise to a theoretically infinite flow velocity (V_{LE}) and a force ($\boldsymbol{F}_{LE}$) at the leading edge of a thin aerofoil (figure 1). The perpendicular and parallel components of the leading-edge force with respect to the camberline direction at the leading edge give the normal ($F_{N,LE}$) and suction ($F_{S,LE}$) forces, respectively. While the normal component of the force can either be positive or negative, depending on the location of the stagnation point and direction of the flow around the aerofoil's leading edge, the suction force always acts in the forward (positive) direction on the aerofoil, as illustrated in figures 1(*a*) and 1(*b*). When the stagnation point coincides with the leading edge of the camberline, the suction force is zero.

Following the unsteady thin-aerofoil theory of Katz & Plotkin (2001) as implemented in Ramesh *et al.* (2013, 2014), the chordwise distribution of the time-dependent vortex-sheet

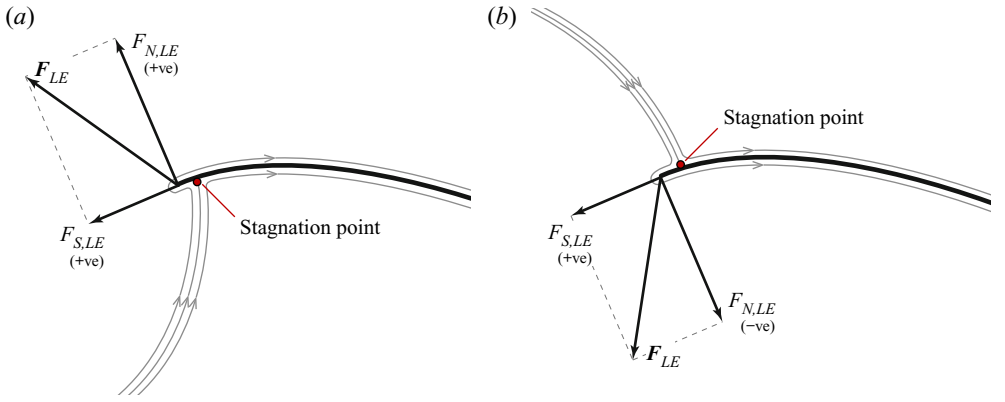

FIGURE 1. Depiction of flow around, and forces on, the leading edge of a thin aerofoil. (*a*) Stagnation point on the lower surface. (*b*) Stagnation point on the upper surface.

strength over the aerofoil, $\gamma(x, t)$, is expressed as a Fourier series as

$$\gamma(\theta, t) = 2U_{ref}\left[A_0(t)\frac{1+\cos\theta}{\sin\theta} + \sum_{n=1}^{\infty} A_n(t)\sin(n\theta)\right], \tag{2.1}$$

where θ is a variable of transformation related to the chordwise coordinate x as

$$x = \frac{c}{2}(1-\cos\theta), \tag{2.2}$$

and $A_0(t), A_1(t), \ldots, A_n(t)$ are the time-dependent Fourier coefficients, c is the aerofoil chord, t is time and U_{ref} is the reference velocity. This reference velocity is usually invariant with time, and is selected based on the problem. In the current formulation, U_{ref} is set equal to the forward velocity, which is the component of the aerofoil's velocity in the negative X direction. Although recent research efforts (Xia & Mohseni 2017; Epps & Greeley 2018; Epps & Roesler 2018; Taha & Rezaei 2019) have provided updates to the Kutta condition at the trailing edge, the current formulation, which is based on the approach of Katz and Plotkin (Katz & Plotkin 2000), assumes zero vortex-sheet strength at the trailing edge, and implicitly enforces the Kutta condition by imposing a zero vortex strength at each time step at the trailing edge. The Fourier coefficients are determined using the instantaneous local downwash on the aerofoil due to all bound and shed vorticity by enforcing the boundary condition that the flow must remain tangential to the aerofoil surface:

$$A_0(t) = -\frac{1}{\pi}\int_0^{\pi}\frac{W(x,t)}{U_{ref}}\,\mathrm{d}\theta, \tag{2.3}$$

$$A_n(t) = \frac{2}{\pi}\int_0^{\pi}\frac{W(x,t)}{U_{ref}}\cos(n\theta)\,\mathrm{d}\theta. \tag{2.4}$$

It has been known for several decades that the onset of separation at the leading edge is governed by criticality of flow parameters at the leading edge. Several researchers (Evans & Mort 1959; Beddoes 1978; Ekaterinaris & Platzer 1998; Jones & Platzer 1998; Morris & Rusak 2013) have correlated leading-edge flow criticality to onset of leading-edge separation and/or static/dynamic stall. The LESP idea of Ramesh *et al.* (2014), inspired

in part by these works, was the result of the search for an appropriate parameter that could be determined as a part of an unsteady aerofoil theoretical calculation.

The LESP is a measure of the suction at the leading edge, which is correlated with the flow velocity around the leading edge, V_{LE}. Ramesh *et al.* (2014) observed that the determining factor for the leading-edge suction and the flow velocity at the leading edge (V_{LE}) for an aerofoil is the circulation at the leading edge, $\gamma(0, t)$, which is represented by the first coefficient $A_0(t)$. Furthermore, using matched asymptotic expansion, Ramesh (2020) showed that V_{LE} is directly proportional to the A_0 coefficient in (2.1) as

$$V_{LE} = \sqrt{\frac{2}{r}} U_{ref} A_0, \tag{2.5}$$

where r is the aerofoil leading-edge radius non-dimensionalized by the chord. It may therefore be argued that the instantaneous A_0 value could serve as the LESP. The instantaneous LESP, denoted generally by $\mathcal{L}$, at any time instant is therefore set equal to the value of $A_0(t)$ at that time. Because A_0 is defined using the reference velocity, U_{ref}, this LESP is based on the reference velocity, and is denoted specifically by $\mathcal{L}^{ref}$ (to distinguish it from an updated LESP that is introduced later). We get

$$\mathcal{L}^{ref}(t) = A_0(t) \tag{2.6}$$

with a positive value of $\mathcal{L}^{ref}$ corresponding to when the stagnation point is on the lower surface (figure 1*a*) and a negative value when the stagnation point is on the upper surface (figure 1*b*).

2.2. *The LESP hypothesis for LEV initiation*

As discussed by Katz (1981), real aerofoils have rounded leading edges which can support some suction even when the stagnation point is away from the leading edge. The amount of suction that can be supported is dependent on the aerofoil shape and the operating Reynolds number. Drawing on the observation that the LESP is a measure of the suction/velocity at the leading edge, Ramesh *et al.* (2014) made the logical choice to develop a correlation for initiation of LEV formation to be based on the LESP. The advantage of this approach is that the instantaneous $\mathcal{L}^{ref}$ can be calculated for any unsteady motion from unsteady thin-aerofoil theory.

The LESP hypothesis proposed by Ramesh *et al.* (2014) is that, for a given aerofoil and Reynolds number combination, the critical LESP, which is the $\mathcal{L}^{ref}$ value corresponding to LEV initiation, is independent of motion kinematics. This hypothesis is based in part on the argument that for a rounded leading edge of an aerofoil that is operating at a given chord Reynolds number, attached flow around the leading edge is supported so long as leading-edge suction is below a critical value. When this critical value is exceeded, the flow at the leading edge will separate, resulting in the shedding of vorticity from the leading edge. Because the LESP is a motion-independent, non-dimensional measure of the leading-edge suction, it should be a good predictor of LEV initiation for any motion. The major benefit of this hypothesis being true is that the critical LESP (i.e. $\mathcal{L}^{ref}_{crit}$) can be determined for one motion from CFD or experiment and can then be used for prediction of LEV initiation for any other motion.

As mentioned in the work of Ramesh *et al.* (2014), an important limitation of the LESP hypothesis is that the $\mathcal{L}^{ref}$ in that approach is determined using inviscid/attached-flow theory (unsteady thin-aerofoil theory), in which the flow over the aerofoil surfaces is assumed to be attached. Thus, as discussed by Ramesh *et al.* (2017), in situations

characterized by trailing-edge flow separation, this 'inviscid LESP' is unlikely to be a true measure of the leading-edge suction. Furthermore, the $\mathcal{L}^{ref}_{crit}$ value derived from unsteady inviscid theory for high pitch-rate motions with negligible trailing-edge boundary-layer separation is not applicable for much lower pitch-rate motions where trailing-edge flow separation is present. The inability of the inviscid LESP to account for the effects of trailing-edge separation was postulated as the reason for the small variation of $\mathcal{L}^{ref}_{crit}$ with pitch rate observed in Ramesh *et al.* (2017). With a new approach to determine the 'viscous LESP' using RANS CFD solutions in the current work, an important aim is to study the viscous $\mathcal{L}^{ref}_{crit}$ behaviour to examine if accounting for the effects of trailing-edge separation will collapse the viscous $\mathcal{L}^{ref}_{crit}$ values for all motions into a small range, irrespective of whether or not boundary-layer separation is present during initiation of LEV formation.

2.3. *Previous hypothesis for the behaviour of LESP after LEV initiation*

In the LDVM low-order method algorithm, Ramesh *et al.* (2014) assumed that once $\mathcal{L}^{ref}$ reaches $\mathcal{L}^{ref}_{crit}$ and LEV shedding starts, the LESP remains constant at $\mathcal{L}^{ref}_{crit}$ until termination of LEV formation. During the LEV shedding process, the strength of the discrete LEV shed during any time step is determined so that the $\mathcal{L}^{ref}$ after the discrete LEV is shed is brought to this $\mathcal{L}^{ref}_{crit}$ value. LEV shedding is terminated once the instantaneous LESP value drops below $\mathcal{L}^{ref}_{crit}$.

The justification to hold the LESP at its predetermined critical value during the shedding process was based in part on the argument proposed by Katz (1981) that leading edges hold a certain amount of suction even when flow is separated. Based on the understanding at that time, it sounded like a reasonable argument that the leading edge had a capacity to hold a certain amount of suction even during LEV shedding, and the excess would be shed as vorticity. Furthermore, there did not seem to be any other guidance on how the suction behaves post-LEV initiation. Finally, and most importantly, when that hypothesis was implemented in the LDVM, the predictions for flow and forces agreed well with CFD and experimental results for all cases (Ramesh *et al.* 2014), which were at low Reynolds numbers of 100 000 and below. One of the objectives of the current work is to carefully test this hypothesis given that the viscous LESP is being determined in the current work using RANS CFD solutions and experimental data.

3. Methodology

In this section, a brief description of the unsteady RANS (URANS) CFD code used in this work is presented in § 3.1, followed by the validation of the numerical scheme with existing experimental data in § 3.2. A procedure to obtain the suction force and LESP from computational pressure distributions is provided in § 3.3. An improved approach to determine LEV initiation from CFD and experimental methods is discussed in § 3.4.

3.1. *CFD method*

CFD calculations were performed using North Carolina State University's REACTMB-INS code, which solves the time-dependent incompressible Navier–Stokes equations using a finite-volume method. The governing equations are written in arbitrary Lagrangian/Eulerian form, which enables the motion of a body-fitted computational mesh in accord with prescribed rate laws. Spatial discretization of the inviscid fluxes uses a low-diffusion flux-splitting method valid in the incompressible limit (Cassidy, Edwards

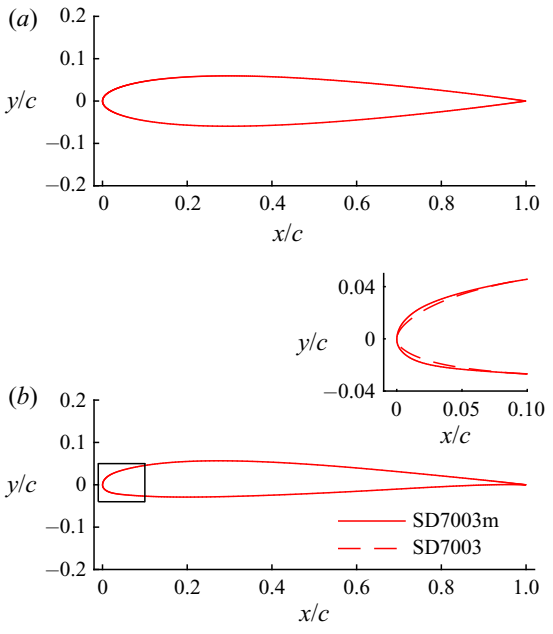

FIGURE 2. (*a*) NACA0012 and (*b*) SD7003m aerofoil geometries.

& Tian 2009). This method is extended to higher-order spatial accuracy using piecewise parabolic method interpolations of the primitive variables $[p, u, v, w]^{\mathrm{T}}$ and transported variable for the S-A model, $\tilde{\nu}$. Viscous terms are discretized using second-order central differences. A dual time-stepping method is used to integrate the equations in time. An artificial compressibility technique, discretized in a fully implicit fashion and solved approximately using ILU decomposition, is used to advance the solution in pseudo-time. Typically, eight sub-iterations per physical time step were needed to reduce the residual errors two orders of magnitude. The Spalart–Allmaras model (Spalart & Allmaras 1992), as implemented by Edwards & Chandra (1996), is used for turbulence closure. The geometries for the two aerofoils used in this work, NACA 0012 and SD7003m, are shown in figure 2. The SD7003m is a modified version of the original SD7003 (Selig, Donovan & Fraser 1989), in which the leading-edge radius is twice that of the original SD7003. Two-dimensional body-fitted O-grids for the NACA 0012 and SD7003m aerofoils containing 140 400 and 92 400 cells, respectively, were generated. Two additional high-density grids for the NACA 23012 and SD7003 aerofoils, containing 284 400 and 108 900 cells, respectively, were generated for validation purposes. The wall y^+ for all the grids generated in the current study was < 5. Additionally, a grid sensitivity study, carried out to ensure grid convergence, showed that decreasing the y^+ to a tenth of that used in the final grids does not alter the results noticeably.

3.2. *CFD validation*

Three test computations were performed to establish the accuracy of the numerical code. Steady simulations were performed for the NACA 0012 aerofoil at a free stream Reynolds number (Re) of 2.5 million and the computed coefficient of lift (C_l) variation with angle of attack (α) was compared with experimental data from Carr *et al.* (1977). The results in figure 3 show that computed C_l is within 5 % of experimental data for all pre-stall

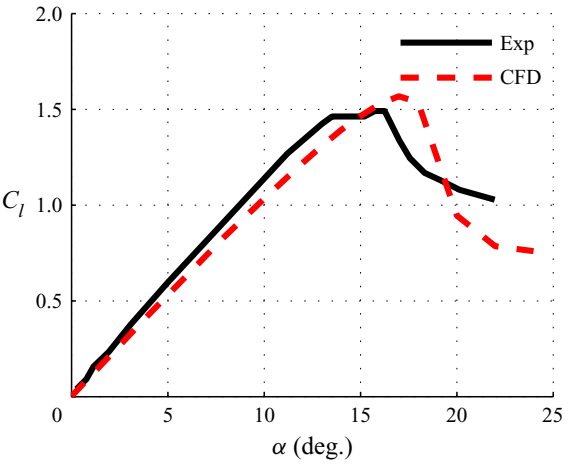

FIGURE 3. Comparison for a stationary aerofoil: steady C_l vs α from computations compared with experimental results of Carr *et al.* (1977) for the NACA 0012 aerofoil at $Re = 2.5 \times 10^6$.

angles of attack. The CFD overpredicts the stall angle by approximately 1 degree and maximum C_l by approximately 0.08. Next, the NACA 23012 aerofoil pivoted at the quarter chord was simulated for an unsteady sinusoidal motion ($20^\circ \pm 10^\circ \sin(\Omega t)$, where Ω is the angular frequency) at a free stream Reynolds number of 1.5 million and reduced frequency ($k = \Omega c/(2U)$) of 0.10, where U is the free stream velocity in this situation. The computed C_l vs α is compared with experimental data from Leishman (1990) in figure 4. The results show that LEV initiation, generally associated with the nonlinear increase in C_l, occurs at a higher angle of attack in the computations. The computational and experimental results exhibit similar trends after lift stall has occurred. Lastly, an unsteady simulation was performed for the SD7003 aerofoil at a free stream Reynolds number of 30 000 and pivoted about the leading edge at a non-dimensional pitch rate ($K = \dot{\alpha}c/(2U)$) of 0.11, where $\dot{\alpha}$ is the dimensional pitch rate, for a pitch-up-hold-return motion defined using the Eldredge function (Eldredge *et al.* 2009; Eldredge & Wang 2011). Figure 5 compares computed C_l vs t^* data with experimental data obtained from the US Air Force Research Laboratory's Horizontal Free-Surface Water Tunnel (Ramesh *et al.* 2014), where t^* is the convective time given by $t^* = tU/c$. The computed C_l agrees well with experiment in the pitch-up phase but is slightly overpredicted in the hold and return phases of the motion. The computation also correctly captures the time instants and intensities of the spikes due to apparent-mass effects.

3.3. *Determination of suction force and LESP from CFD*

The determination of the leading-edge suction force and LESP for a thin aerofoil from unsteady theory was discussed in § 2.1. Because the theory assumes attached flow over the aerofoil (i.e. no trailing-edge separation), that LESP is referred to in this work as the 'inviscid LESP.' Motivated by the desire to understand the behaviour of the suction force on rounded leading-edge aerofoils in real flows, an approach was developed in the current work to calculate the suction force from RANS CFD solutions. Because the LESP calculated from this CFD-derived suction force accounts for trailing-edge separation and other viscous phenomena, this LESP is referred to as the 'viscous LESP.' Gaining an understanding of the behaviour of the viscous LESP would allow for careful evaluation of

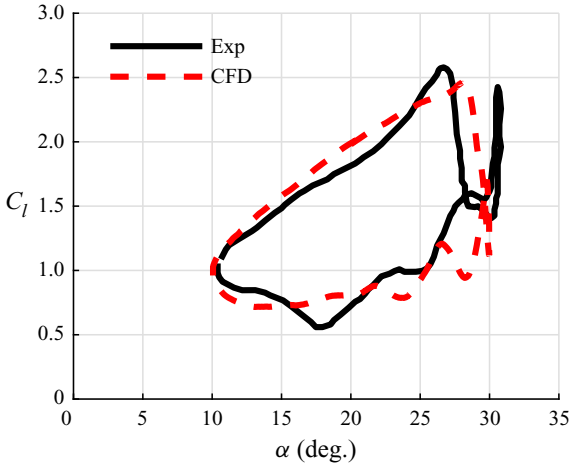

FIGURE 4. Comparison for a sinusoidal pitching aerofoil: computed C_l vs α compared with the experimental results of Leishman (1990) for the NACA 23012 aerofoil at $Re = 1.5 \times 10^6$, $k = 0.10$, $\alpha(t) = 20^\circ \pm 10^\circ \sin(\Omega t)$.

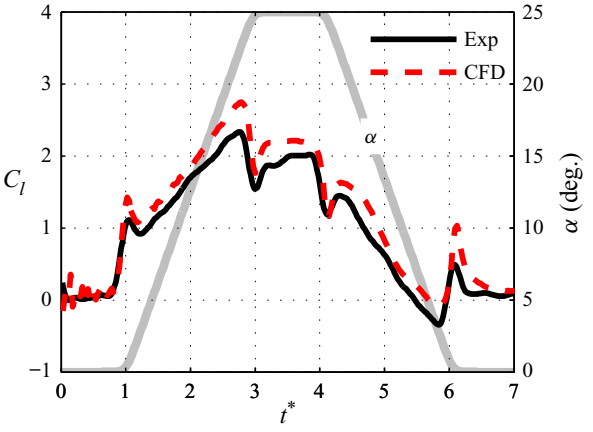

FIGURE 5. Comparison for a low-Re pitching aerofoil: computed C_l vs t^* compared with experimental results in Ramesh *et al.* (2014) for the SD7003 aerofoil at $Re = 30\,000$, $K = 0.11$, $\alpha_{max} = 25^\circ$.

the LESP-related hypotheses in §§ 2.2 and 2.3, and enable improved modelling of LEV shedding.

When the stagnation point is not at the geometric leading edge of the aerofoil, the flow is forced to travel around the rounded leading edge. This flow curvature gives rise to a low-pressure region near the leading edge. As done in § 2.1, the net force acting on the leading edge is resolved into components acting along and normal to the direction of the camberline at the leading edge. The component of force along the camberline is often a 'suction' force acting in the forward direction. The curvature of the streamlines around the leading edge, the resulting suction near the leading edge and the leading-edge forces are illustrated in figure 6. In the current work, the leading-edge force on the aerofoil is calculated from CFD by integrating the surface pressure on the forward portion of the aerofoil from the leading edge to a predefined chordwise location, denoted

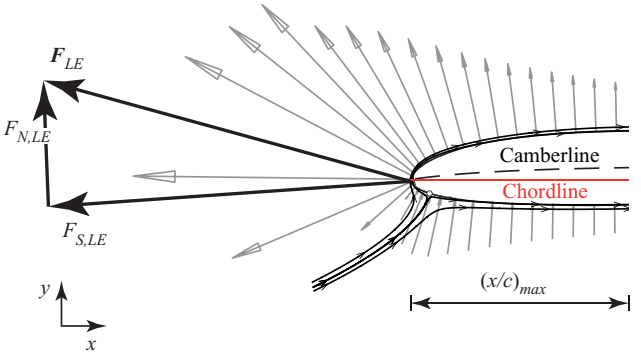

FIGURE 6. Representation of the leading-edge force, $\boldsymbol{F}_{LE}$, resolved into suction force ($F_{S,LE}$) parallel to the camberline, and normal force ($F_{N,LE}$) perpendicular to the camberline at the leading edge.

by $(x/c)_{max}$. This force is then split into its suction and normal components, which when non-dimensionalized by the dynamic pressure ($q_{ref} = \rho U_{ref}^2/2$, where ρ is the free stream density) and chord, give the coefficients of suction, $C_{s,LE}^{ref}$, and normal force, $C_{n,LE}^{ref}$, on the leading edge. The superscript '*ref*' is used here to differentiate these force coefficients from those defined later using a different velocity:

$$C_{s,LE}^{ref} = F_{S,LE}/q_{ref}c, \tag{3.1}$$

$$C_{n,LE}^{ref} = F_{N,LE}/q_{ref}c. \tag{3.2}$$

Figure 7 shows the temporal variation of the coefficient of suction (referred to as C_s^{ref} instead of $C_{s,LE}^{ref}$ from here onward) calculated from the unsteady RANS CFD solution using various values of $(x/c)_{max}$ for a NACA 0012 aerofoil undergoing a pitch-up-return motion with $K = 0.1$ at a Reynolds number of 3 million. We observe that for $(x/c)_{max} \geq 0.30$, the suction force is relatively independent of the selected $(x/c)_{max}$. We note that the x/c location of the maximum thickness of the NACA 0012 aerofoil is at 0.30. While there is no theoretical guidance on a correct value of $(x/c)_{max}$ to use for integration of CFD pressures to calculate C_s^{ref}, we have found that using the $(x/c)_{max}$ corresponding to the maximum thickness location on the chord works well. The calculated value of C_s^{ref} is relatively insensitive to the chosen $(x/c)_{max}$ around this value because the aerofoil surfaces are typically nearly parallel to the chord in the vicinity of the maximum thickness location and the pressure contributions from these portions of the aerofoil to the suction force are small. Thus, the leading-edge suction and normal forces in this work are defined as the appropriate components of the net force acting on the forward portion of the aerofoil from the leading edge to the x/c for the maximum thickness location. Also co-plotted in figure 7 is the time variation of the inviscid C_s^{ref} calculated from the unsteady aerofoil theory for this motion. We see that the CFD-derived C_s^{ref} agrees well with the theoretical C_s^{ref} for small pitch angles at which the flow on the upper surface is fully attached, which shows that the CFD-derived C_s^{ref} is a good equivalence for the theoretical C_s^{ref} in attached-flow conditions. At $t^* > \approx 14$, which corresponds to $\alpha > \approx 42$ degrees, when LEV shedding is active, the theoretical C_s^{ref} is seen to be much larger than the CFD-derived C_s^{ref}. This large difference is because the theoretical C_s^{ref} does not account for any viscous effects, while the CFD-derived C_s^{ref} is a measure of the suction force from simulations of the real viscous flow.

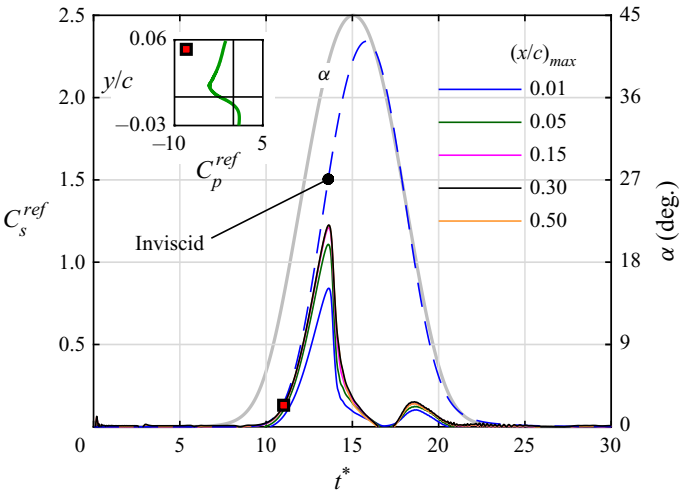

FIGURE 7. Time variation of C_s^{ref} for representative motions for various $(x/c)_{max}$ values used for the integration.

The inset in figure 7 shows the surface pressure coefficient (C_p^{ref}) variation plotted against y/c for the forward portion of the aerofoil (for $0 \leq x/c \leq 0.30$) at an example time instant of $t^* = 12$ when the flow is fully attached. This pressure coefficient is defined using the reference dynamic pressure as $C_p^{ref} = (p - p_\infty)/q_{ref}$. This plot has the y/c scale on the vertical axis so that the area inside the curve gives a visual representation of the leading-edge suction force acting in the horizontal (chordwise) direction. The vertical distribution of the C_p^{ref} along the y/c in this plot provides information on whether the suction is concentrated on the upper or lower surface of the aerofoil. Such C_p vs y/c plots are used later in this manuscript to discuss the suction behaviour for various situations.

As shown by Ramesh *et al.* (2013), aerofoil theory gives the relationship between C_s^{ref} and LESP as

$$C_s^{ref} = 2\pi(\mathcal{L}^{ref})^2. \tag{3.3}$$

As discussed in § 2.1, the suction force ($F_{S,LE}$) and the suction-force coefficient (C_s^{ref}), when calculated from theory, cannot be negative. However, because C_s^{ref} calculated from CFD may not perfectly match up with that from ideal flow, there are a few situations in which, when the theoretical C_s^{ref} value is zero or a small positive value, the CFD-derived C_s^{ref} has a small negative value. To ensure compatibility with the theoretical C_s^{ref} and to avoid problems when calculating the LESP, the CFD-derived LESP is set to zero at the few time instants when the viscous C_s^{ref} has a negative value. Furthermore, the sign of the LESP is set to be the same as that of the $C_{n,LE}^{ref}$, so that positive $C_{n,LE}^{ref}$ is assumed to correspond to a flow with stagnation point on the lower surface, and vice versa. Thus, the CFD-derived viscous LESP is calculated from the CFD-derived C_s^{ref} as

$$\mathcal{L}^{ref} = \begin{cases} \mathrm{sgn}(C_{n,LE}^{ref})\sqrt{\frac{C_s^{ref}}{2\pi}}, & \text{for } C_s^{ref} > 0, \\ 0, & \text{for } C_s^{ref} \leqslant 0. \end{cases} \tag{3.4}$$

The time histories of the viscous C_s^{ref} and $C_{n,LE}^{ref}$ calculated from integration of the CFD pressure distribution over the leading-edge region of a NACA 0012 aerofoil at a

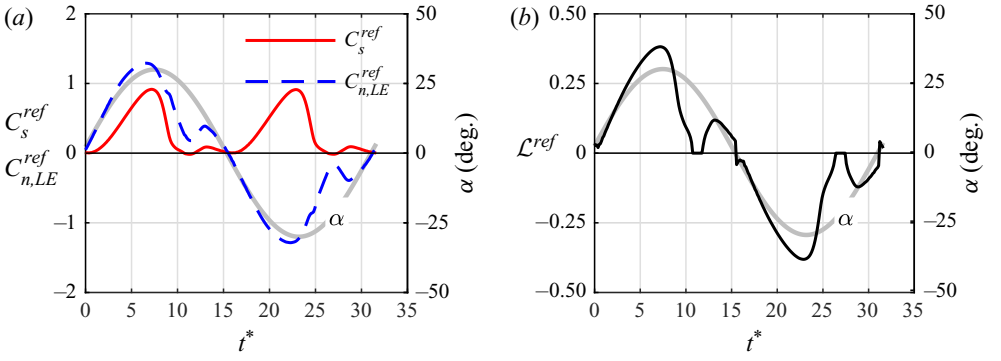

FIGURE 8. Variation of CFD-derived leading-edge quantities for an example sinusoidal motion: (*a*) viscous C_s^{ref} and $C_{n,LE}^{ref}$, and (*b*) viscous $\mathcal{L}^{ref}$ vs t^*.

Reynolds number of 3 million, undergoing sinusoidal pitching ($\alpha(t) = 0^\circ \pm 30^\circ \sin(\Omega t)$) with a reduced frequency of $k = \Omega c/(2U_{ref}) = 0.1$ and pivoted at the half-chord is shown in figure 8(*a*). The viscous LESP for this case, calculated using (3.4), is shown in figure 8(*b*). The few flat spots and abrupt jumps when the LESP is close to zero are the result of conversion of viscous C_s^{ref} to viscous LESP using (3.4). These flat spots are inconsequential because the flow events related to leading-edge stall occur only when the LESP is at high values.

3.4. *Improved determination of LEV initiation from CFD and experiment*

An important part of the current work is to examine the events leading to LEV formation for multiple aerofoils, a large set of motion kinematics, and over a range of Reynolds numbers. Although LEV initiation can be qualitatively inferred from CFD flow-field images by marking the time instant at which the first sign of an LEV structure appears during a motion, such a process is subjective and results in noise when comparisons are made for a large number of cases. Furthermore, it is desirable that the approach involve surface quantities and be straightforward to implement so that the data processing can be automated. In earlier work involving low-Reynolds-number unsteady aerofoil flows, a signature in the surface skin-friction coefficient (C_f^{ref}, defined using U_{ref}) distribution was used for identifying the time instant of LEV initiation (Ramesh *et al.* 2014; Hirato *et al.* 2019). An improved approach that works well at both low and high Reynolds numbers is presented in this section. In this illustration, a NACA 0012 aerofoil undergoing a pitch-up motion about the quarter chord at $K = 0.4$ is considered at Reynolds numbers of 30 000 and 3 million. Results from CFD at five time instants are considered to illustrate the events from slightly before to slightly after LEV formation.

For the flow field results from CFD presented in this section and in the remainder of the paper, the colour bars used for all the non-dimensional velocity-magnitude plots (contours of U_{mag}/U_∞, where U_{mag} is the velocity magnitude) and non-dimensional vorticity plots (contours of $\omega c/U_\infty$, where ω is the vorticity) are shown in figure 9.

Figure 10 shows the motion history and the time-variation of the inviscid and viscous LESP for the low-Reynolds-number case ($Re = 30\,000$). Only a small time range from slightly before to slightly after initiation of LEV formation is presented here. It is emphasized that the inviscid LESP variation is calculated using attached-flow assumptions, with neither LEV shedding (unlike in the LDVM low-order method (Ramesh

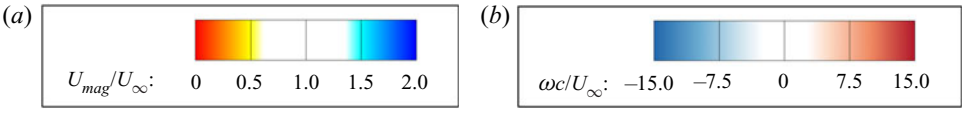

FIGURE 9. Colour bars for the CFD flow field plots presented in this paper: (*a*) non-dimensional velocity magnitude (U_{mag}/U_∞) and (*b*) non-dimensional vorticity ($(\omega c)/U_\infty$).

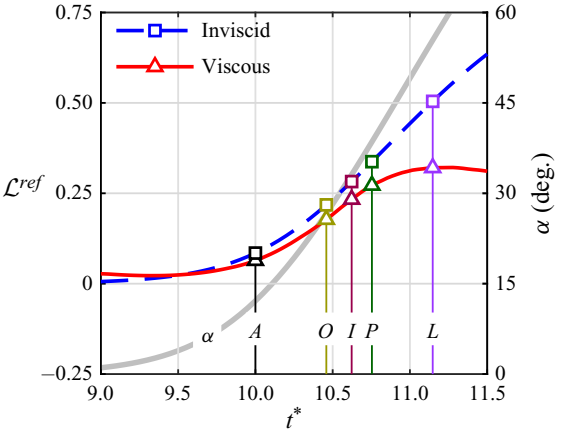

FIGURE 10. Events around LEV initiation for the low-*Re* case: variation of $\mathcal{L}^{ref}$ with t^* for an unsteady NACA 0012 aerofoil at $Re = 30\,000$, $K = 0.4$, pivoted at the half-chord.

et al. 2014)) nor trailing-edge separation (unlike in the unsteady trailing-edge separation method (Narsipur, Gopalarathnam & Edwards 2019)), and is therefore valid only until the onset of LEV shedding even though the LESP variation is plotted for the entire motion. The time instants for the five events are marked in this plot. For each of the five events, figure 11 shows in each row the vorticity contours around the entire aerofoil, a zoomed-in plot of the vorticity variation around the leading-edge region for $0 \leqslant x/c \leqslant 0.25$, the surface-$C_f^{ref}$ for the leading-edge region and a plot of the leading-edge C_p^{ref} vs y/c. The events are labelled as follows: 'A' for attached flow; 'O' for onset of flow reversal on the surface, identifiable by the first occurrence of a small region of negative C_f^{ref} near the leading edge; 'I' for the first appearance of an inflection point within the negative-C_f^{ref} region; 'P' for the first instant at which the inflection grows to become a positive spike within the negative-C_f^{ref} region; and 'L' for the first instant at which the LEV structure is clearly identifiable from the vorticity contour. Mathematically, the inflection point for event I is identified as the first time instant in the motion at which the second derivative of the surface-C_f^{ref}, $\partial^2 C_f^{ref}/\partial(x/c)^2$, near the leading edge becomes negative. In earlier work (Ramesh *et al.* 2014), the C_f^{ref} signature from CFD results associated with the P event was used as the quantitative criterion to determine the instant of LEV initiation for any given motion. This signature works well for low-Reynolds-number situations.

Figure 12 shows the motion history and the time variations of inviscid and viscous LESP for the high-Reynolds-number case ($Re = 3$ million). Each row of figure 13 shows the vorticity plot around the aerofoil, vorticity around the leading-edge region ($0 \leqslant x/c \leqslant 0.25$), the surface-$C_f^{ref}$ for the leading-edge region and the C_p^{ref} variation vs y/c

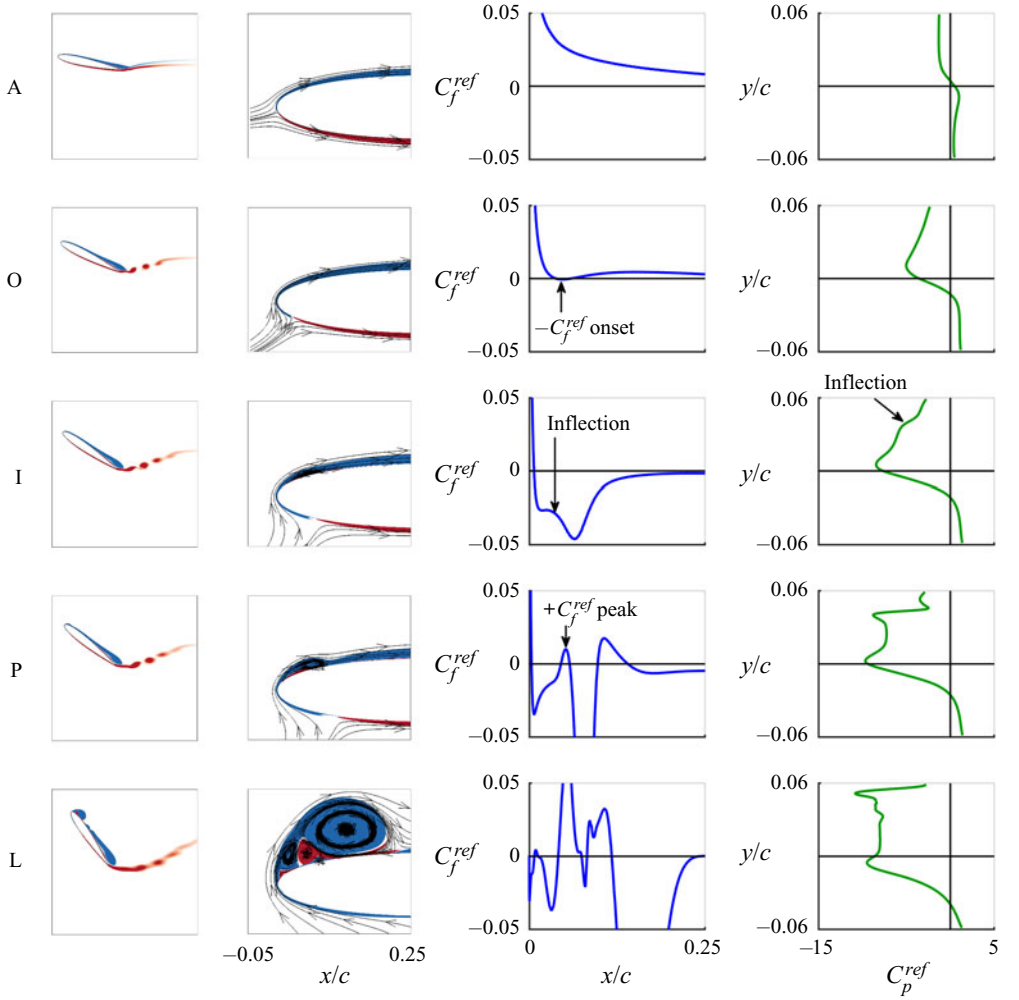

FIGURE 11. Events around LEV initiation for the low-*Re* case: LEV events for an unsteady NACA 0012 aerofoil at $Re = 30\,000$, $K = 0.4$, pivoted at the half-chord.

for the five events. A noticeable difference between the low-Reynolds-number behaviour (figures 10 and 11) and the high-Reynolds-number behaviour (figures 12 and 13) is that, in the high-Reynolds-number case there is already evidence of an LEV structure in the vorticity plot for event P. This behaviour is consistently seen in all the high-Reynolds-number CFD results from the current work, and indicates that event P is not the best choice for LEV initiation for these cases. Based on these observations, event I – the instant at which an inflection point is first observed within the negative-C_f^{ref} region near the leading edge, is chosen as the event corresponding to LEV initiation for both low- and high-Re cases. It is emphasized that the surface-C_f^{ref} signature corresponding to event I is merely used as a consistent identifier of the time instant of LEV initiation from CFD results for the many cases studied in this work. Although the overall observations presented here are somewhat specific to the RANS CFD method used in this work and earlier related efforts (Ramesh *et al.* 2013, 2014; Hirato *et al.* 2019), they are in general

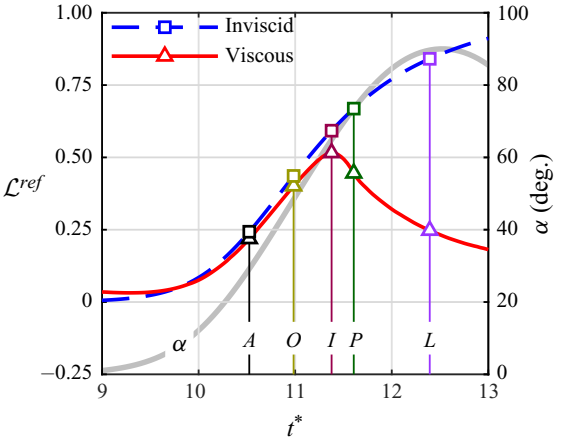

FIGURE 12. Events around LEV initiation for the high-*Re* case: variation of $\mathcal{L}^{ref}$ with t^* for an unsteady NACA 0012 aerofoil at $Re = 3 \times 10^6$, $K = 0.4$, pivoted at the half-chord.

agreement with the LEV-formation flow physics discussed by other researchers (Visbal & Shang 1989; Choudhuri *et al.* 1994; Mulleners & Raffel 2012; Gupta & Ansell 2019).

Finally it is worth mentioning that, in both low-*Re* and high-*Re* cases, between events O and I, there is also the appearance of an inflection point in the C_p^{ref} vs y/c variations. This observation points to the potential use of the inflection in the C_p^{ref} distribution as a signature for LEV initiation from experimental data in which surface shear stress is not measured, but surface-C_p^{ref} distributions are available from a pressure-tapped aerofoil model. However, a reasonably high density of pressure taps would be required to detect the occurrence of the inflection point.

4. Motions

For the current work, a total of 115 cases, divided between two aerofoils (NACA 0012 and SD7003m, shown earlier in figure 2), two Reynolds numbers, five pivot locations and multiple pitch rates, were simulated using the URANS CFD code described in § 3.1, and are listed in table 1. The five pivot locations correspond to the leading edge, quarter chord, half chord, three quarter chord and trailing edge, respectively denoted by LE, QC, HC, TQ, and TE in the figure legends. All motions are of pitch-up-return type generated using Eldredge's canonical formulation (Eldredge *et al.* 2009; Wang & Eldredge 2013). A smoothing function, $G(t)$, is defined as

$$G(t) = \ln\left[\frac{\cosh(aU_\infty(t-t_1)/c)\cosh(aU_\infty(t-t_4)/c)}{\cosh(aU_\infty(t-t_2)/c)\cosh(aU_\infty(t-t_3)/c)}\right], \tag{4.1}$$

where a is a smoothing parameter from Granlund, Ol & Bernal (2011), given by

$$a = \frac{\pi^2 K}{2\alpha_{amp}(1-\sigma)}, \tag{4.2}$$

and the times t_1 to t_4 are: t_1 = time from reference 0 until the start of the ramp; $t_2 = t_1 + \alpha_{amp}/2K$; $t_3 = t_2 + \pi\alpha_{amp}/4K - \alpha_{amp}/2K$; and $t_4 = t_3 + \alpha_{amp}/2K$, where α_{amp} is the amplitude of the pitching motion and K is the non-dimensional pitch rate. The variation

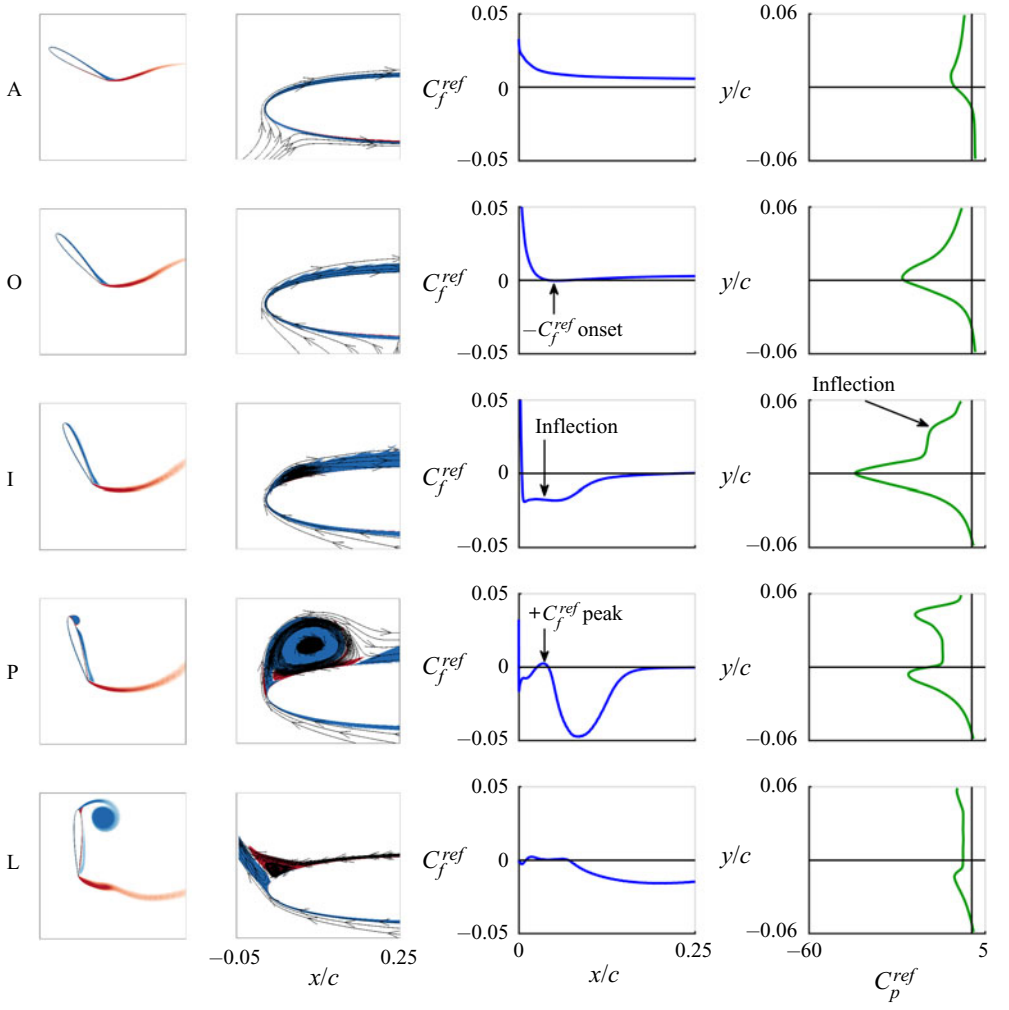

FIGURE 13. Events around LEV initiation for the high-*Re* case: LEV events for an unsteady NACA 0012 aerofoil at $Re = 3 \times 10^6$, $K = 0.4$, pivoted at the half-chord.

Study	Aerofoil	Reynolds Number	Pitch Rate (K)	Pivot
LEV initiation	NACA 0012 SD7003m	3×10^4 3×10^6	0.05–0.6 (medium to high pitch rates)	LE, QC, HC, TQ, TE
No LEV initiation	NACA 0012	3×10^6	0.005–0.01 (low pitch rates)	LE, QC, HC, TQ, TE
Post-LEV behaviour	NACA 0012 SD7003m	3×10^4 3×10^6	0.05–0.6 (medium to high pitch rates)	LE, QC, HC, TQ, TE

TABLE 1. Summary of the cases for which results are presented.

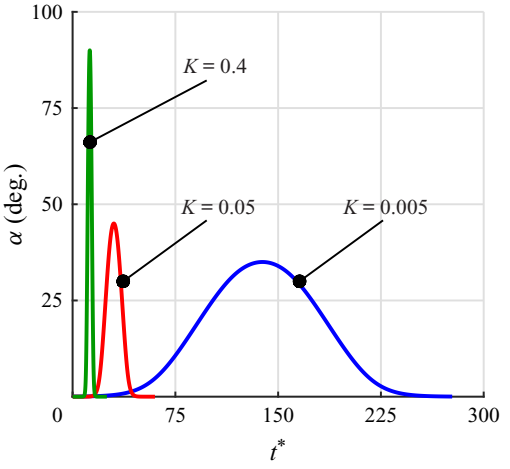

FIGURE 14. Variation of α with t^* for three representative motions: low-K, medium-K, and high-K.

of pitch during the motion is then given by

$$\alpha(t) = \alpha_{amp} \frac{G(t)}{\max(G(t))}. \tag{4.3}$$

Three pitch-up-return motions representative of a low pitch-rate motion ($K = 0.005$), a moderate pitch-rate motion ($K = 0.05$) and a high pitch-rate motion ($K = 0.4$) are plotted in figure 14. It is seen that the motions are smoothed pitch-up-return motions in which the $\mathrm{d}\alpha/\mathrm{d}t^*$ varies during the pitch-up and pitch-down portions of the motions.

5. Variation of $\mathcal{L}^{ref}$ at LEV initiation

Aerofoils with rounded leading edges evince LEV formation at medium and high pitch rates, as observed for the NACA 0012 and SD7003m aerofoils in the current work. In this first set of results, the variation of LESP at the time instants corresponding to events O and I for the 25 medium and high pitch-rate cases are studied to examine if the critical value of LESP is independent of motion kinematics. The earlier results of Ramesh *et al.* (2014) showed that, for low Reynolds numbers (*Re* in the range of 1000 to 100 000) and pitch, plunge, and combination motions at medium to high rates, the critical LESP was largely motion independent. The systematic study of pitching motions in Ramesh *et al.* (2017) further showed that, although there is a small variation in critical LESP with K over the range $0.05 \leq K \leq 0.4$, the use of a single average value of critical LESP in a low-order model such as LDVM (Ramesh *et al.* 2014) produced an acceptable error of ± 2.5 degrees in the predicted pitch angle for LEV initiation. For pitching aerofoils, LEV formation is accompanied by significantly greater trailing-edge separation for low-K motions than for high-K motions. In these earlier works, however, the inviscid LESP was calculated using attached-flow theory which does not account for any separation. The small, but noticeable, variation in critical LESP with K was attributed in Ramesh *et al.* (2017) to the different extents of trailing-edge separation with pitch rate.

The study in the current effort differs from the earlier works in three main respects: (i) viscous LESP, derived from CFD solutions, which, therefore, takes into account the effects of trailing-edge separation, are used; (ii) the range of motion parameters is

expanded to include more pivot locations and a higher K value of 0.6; and (iii) the variation of LESP at events O and I is also examined at a high Reynolds number of 3 million (in addition to the low Reynolds number of 30, 000, which is close to those used in Ramesh *et al.* (2014, 2017)).

In this section the variation of $\mathcal{L}^{ref}$ with motion parameters, x_p/c and K, are presented for the two aerofoils, first for the low Reynolds number of 30 000 in § 5.1 and next for the high Reynolds number of 3 million in § 5.2. Because the motions used in the current work are smoothed pitch ramps having considerable variation of $\dot{\alpha}$ during the motion, these variations for events O and I are plotted against the instantaneous values of $\mathrm{d}\alpha/\mathrm{d}t^*$ for those events rather than against the motion K.

5.1. *Low-Reynolds-number cases*

The values of viscous LESP at events O and I for the 25 medium and high pitch-rate motions for $Re = 30\,000$ are shown in figure 15, with the results for the NACA 0012 and SD7003m aerofoils shown in figures 15(*a*) and 15(*b*), respectively. The data points for event O are shown as open symbols and those for event I are shown as filled symbols. Lines joining the data points for the half-chord pivot cases are included to show the trends of $\mathcal{L}^{ref}$ with $\mathrm{d}\alpha/\mathrm{d}t^*$. An error bar is shown to indicate the typical error in $\mathcal{L}^{ref}$ of 0.015 for each event due to the discrete time steps at which the CFD pressure data is available. Also plotted in figure 15(*b*) are the data points for the critical $\mathcal{L}^{ref}$ vs $\mathrm{d}\alpha/\mathrm{d}t^*$ from Ramesh *et al.* (2017) for the SD7003 aerofoil undergoing pitch-up motions about a quarter-chord pivot at a Reynolds number of 20 000. These data points from Ramesh *et al.* (2017) are the inviscid LESP values for LEV initiation, determined using the LDVM code assuming attached flow, for the time instants corresponding to when the surface-C_f^{ref} signature for event P was observed in the CFD result for pitch-up motions. These data points were also shown in Ramesh *et al.* (2017) to qualitatively agree with experimental results from dye-flow visualization of the corresponding unsteady motions in water-tunnel experiments. This experimental confirmation was achieved by showing that, for each motion, there was a formation of distinct LEV structure in the dye-flow visualization just after the time instant at which LEV initiation was observed from the surface-C_f^{ref} signature in the CFD result. Even though the aerofoil, Reynolds number and the event used for identifying the LEV initiation for this data from Ramesh *et al.* (2017) are all slightly different from those used in the current work for the SD7003m cases, it is seen that the variation in $\mathcal{L}^{ref}$ for event I with instantaneous pitch rate from the current work is very similar to those for the data points from Ramesh *et al.* (2017), except for the small offset in $\mathcal{L}^{ref}$.

Comparing the results for the two aerofoils from the current effort, it is seen that the values and trends are very similar. The $\mathcal{L}^{ref}$ values for the non-half-chord pivot locations for each event are seen to fall within a small range of the corresponding trend line. The two trends lines are seen to have an increase in $\mathcal{L}^{ref}$ of approximately 0.10 for a change in $\mathrm{d}\alpha/\mathrm{d}t^*$ from 0.1 to 1.0. The observation that there is a change in viscous $\mathcal{L}^{ref}$ with pitch rate from the data in the current effort, and that it is nearly the same as the variation in inviscid $\mathcal{L}^{ref}$ from the data of Ramesh *et al.* (2017), shows that this effect of pitch rate on $\mathcal{L}^{ref}$ is not due to different amounts of trailing-edge separation, as postulated in Ramesh *et al.* (2017). Although the critical $\mathcal{L}^{\mathrm{ref}}$ of the trend line is not constant with $\mathrm{d}\alpha/\mathrm{d}t^*$, it is noted that the range of K (and, hence, the range of $\mathrm{d}\alpha/\mathrm{d}t^*$) examined here is very large, with applications spanning from helicopter dynamic stall at the very low values of K to insect and flapping-wing MAV flight at the very high end of the range examined. In practice,

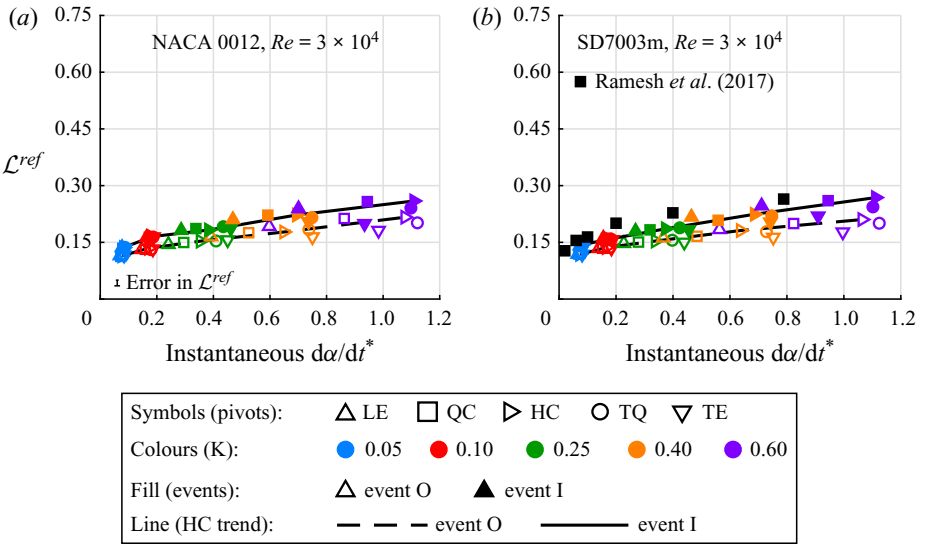

FIGURE 15. LEV initiation at low Reynolds numbers: variation of $\mathcal{L}^{ref}$ at events O and I with instantaneous pitch rate for the (*a*) NACA 0012 and (*b*) SD7003m aerofoils at $Re = 30\,000$. Data points from Ramesh *et al.* (2017) are also included in (*b*).

within the much smaller range of pitch rates typically used in any single application, the critical LESP can be considered as essentially a constant.

5.2. *High-Reynolds-number cases*

The values of $\mathcal{L}^{ref}$ at events O and I for the higher-*Re* cases ($Re = 3$ million) are shown in figures 16(*a*) and 16(*b*) for the NACA 0012 and SD7003m aerofoils, respectively. It is seen that the $\mathcal{L}^{ref}$ values for the high-*Re* cases are, in general, approximately 0.3 higher than those for the low-*Re* cases. The higher $\mathcal{L}^{ref}$ values indicate that, for a given motion, the high-*Re* LEV initiation is delayed to a higher pitch angle compared with the low-*Re* LEV initiation. This behaviour is to be expected, as the predicted level of boundary-layer separation at higher Reynolds numbers is typically delayed compared with lower Reynolds numbers due to the energizing effects of modelled turbulence. In our cases, the turbulence model was applied without a transition model, meaning that the boundary layer is predicted to be turbulent from the leading edge at the higher Reynolds number. Because the $\mathcal{L}^{ref}$ for event I is taken as the critical $\mathcal{L}^{ref}$ for modelling initiation of LEV formation in low-order methods like the LDVM (Ramesh *et al.* 2014), it is noted that the $\mathcal{L}^{ref}_{crit}$ varies with Reynolds number and needs to be determined using CFD computations at the Reynolds number of interest for the problem at hand.

Compared with the low-*Re* variations, the trend lines for the half-chord pivot cases in the high-*Re* results are seen to have much smaller slopes. However, the spread in $\mathcal{L}^{ref}$ values for the other pivot locations relative to the corresponding trend lines is significantly larger than those seen in the low-*Re* cases. This spread in $\mathcal{L}^{ref}$ due to pivot location is especially large for the higher-K cases, and reaches a LESP change of almost 0.3 between the leading-edge and trailing-edge pivot locations for the $K = 0.6$ cases. In comparison, the same change for the low-*Re* case is only 0.05. Furthermore, the variation in $\mathcal{L}^{ref}$ with pitch rate is seen to depend on the pivot location. For the leading-edge pivot cases, for

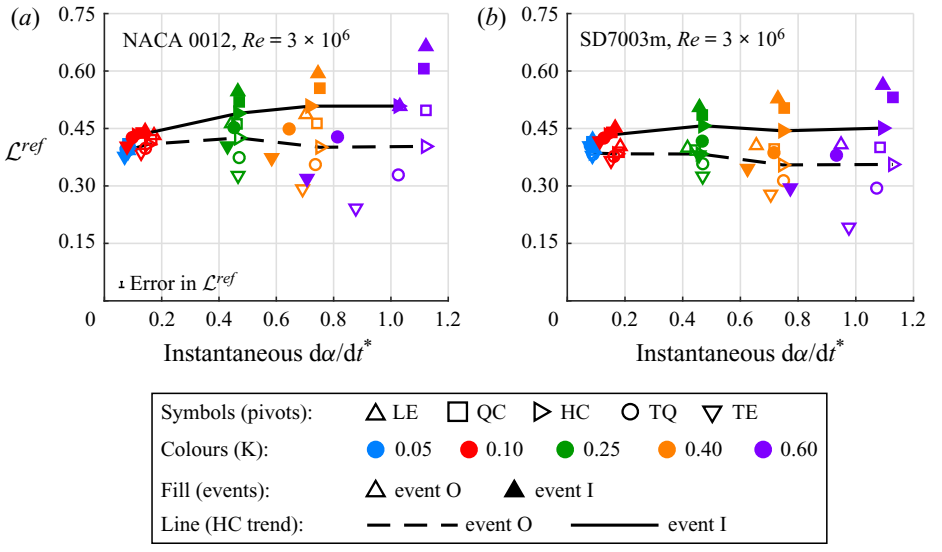

FIGURE 16. LEV initiation at high Reynolds numbers: variation of $\mathcal{L}^{ref}$ at events O and I with instantaneous pitch rate for the (*a*) NACA 0012 and (*b*) SD7003m aerofoils at $Re = 3$ million.

instance, $\mathcal{L}^{ref}$ is seen to increase with pitch rate, while for the trailing-edge pivot cases, the $\mathcal{L}^{ref}$ is seen to decrease with pitch rate. The results show conclusively that the $\mathcal{L}^{ref}$, as defined in the earlier works (Ramesh *et al.* 2014, 2017) and thus far in this paper, fails to have anywhere close to a constant value at either event O or I, negating its utility in low-order prediction of LEV initiation for the high-*Re* situations.

6. An updated LESP formulation using the net velocity

A careful examination was made of the possible reasons for the failure of the original LESP formulation for the high-*Re* cases, leading to large variations in $\mathcal{L}^{ref}$ between motions. This effort led to the realization that the problem was in the use of the single reference velocity, U_{ref}, used in the definition of $A_0(t)$ (2.3) and, therefore, of $\mathcal{L}^{ref}(t)$, which is set equal to $A_0(t)$ (2.6). Because LESP is being used to compare LEV initiation due to unsteady motions with vastly different non-dimensional rates, the traditional approach of using a single reference velocity, U_{ref}, is unlikely to work unless the motion rates are small at LEV initiation. As noted earlier, U_{ref} is set here to the forward speed, U, following normal practice. For an aerofoil that has a high non-dimensional pitch or plunge rate, the magnitude of the net velocity of the aerofoil relative to the undisturbed fluid, which we denote here by U_{net}, could be significantly different from the magnitude of the single reference velocity, U_{ref}. In general, the net-velocity magnitude would also be time varying, $U_{net}(t)$. The pressures, surface shear stresses and loads on the aerofoil, including the leading-edge suction force, are proportional to the square of the net-velocity magnitude. To further illustrate this idea, we consider two unsteady motions of an aerofoil. These two motions comprise the same forward speed, U, and the same reference velocity, $U_{ref} = U$, but one motion has a slow pitch/plunge rate and the other has a fast pitch/plunge rate. To properly compare the instantaneous leading-edge aerodynamic condition at a time instant in the first motion with that at a different time instant in the second motion, it is necessary to use non-dimensional force coefficients and parameters that have been referenced in

each case to the corresponding instantaneous values of the net-velocity magnitude of the aerofoil, $U_{net}(t)$.

It now remains to develop an expression for $U_{net}(t)$ for any given motion. In a general case, the contributions to $U_{net}(t)$ arise not only due to the kinematics, i.e. the velocity of the aerofoil relative to the undisturbed fluid, but also due to velocities induced at the aerofoil due to any vortical structures in the fluid. For the problem at hand, these vortical structures include the wake vorticity that was shed from the trailing edge of the aerofoil. For the purpose of developing a correction to the LESP formulation due to motion kinematics, we assume here that the contributions to $U_{net}(t)$ due to kinematics is significantly larger than those due to the wake vortical structures, allowing us to ignore the latter. The expression for $U_{net}(t)$ is straightforward for plunge motions. For an aerofoil with a horizontal velocity $U(t)$ along the $-x$ direction and a vertical plunge velocity $\dot{h}(t)$ along the positive y direction, the $U_{net}(t)$ is simply: $U_{net}(t) = \sqrt{U(t)^2 + \dot{h}(t)^2}$. For pitch motions, the calculation of $U_{net}(t)$ is more complicated because the velocity due to the pitch rate varies along the chord depending on the distance from the pivot location. In the search for a theoretical basis for the velocity contribution due to the pitch rate, we get some direction from the expression for A_0 from quasi-steady thin-aerofoil theory (QSTAT) (Leishman 2002; Ramesh 2020). This theory provides expressions for the thin-aerofoil theory Fourier terms, lift and pitching-moment coefficients by applying the quasi-steady assumptions of negligible contributions from the wake vorticity. From Ramesh (2020) we get the expression for $A_0(t)$ for a symmetric aerofoil at a pitch angle of $\alpha(t)$ undergoing unsteady motion with a time-varying forward velocity, $U(t)$, upward plunge velocity, $\dot{h}(t)$, and pitch rate $\dot{\alpha}(t)$ about a non-dimensional pivot location x_p/c as

$$A_0(t) = \frac{U(t)}{U_{ref}} \sin\alpha(t) - \frac{\dot{h}(t)}{U_{ref}} \cos\alpha(t) + \frac{\dot{\alpha}(t)c}{U_{ref}} \left(\frac{1}{2} - \frac{x_p}{c}\right). \tag{6.1}$$

The last term of this expression gives the pitch-rate contribution to $A_0(t)$ from QSTAT. We see that this contribution becomes zero when the pivot is at the half-chord location. We also see that the last term is the ratio of the velocity of the half-chord point due to pitch rate to the reference velocity. Because LESP is strongly connected to A_0, the pitch-rate contribution to U_{net} is taken as the velocity of the half-chord point on the aerofoil due to the pitch rate, $\boldsymbol{U}_{pitch}$. Therefore, as illustrated in figure 17, the net velocity is the vector sum of the forward velocity, plunge velocity and the velocity of the half-chord point due to the pitch rate. The ratio U_{net}/U_{ref} can be expressed as

$$\frac{U_{net}(t)}{U_{ref}} = \sqrt{\left[\frac{U(t)}{U_{ref}} + \frac{\dot{\alpha}(t)c}{U_{ref}} \left(\frac{1}{2} - \frac{x_p}{c}\right) \sin\alpha(t)\right]^2 + \left[\frac{\dot{h}(t)}{U_{ref}} - \frac{\dot{\alpha}(t)c}{U_{ref}} \left(\frac{1}{2} - \frac{x_p}{c}\right) \cos\alpha(t)\right]^2}, \tag{6.2}$$

which, for the current work in which $U(t)$ is a constant and $U_{ref} = U$, can be rewritten in terms of non-dimensional pitch rate, $\overset{*}{\alpha} = \partial\alpha/\partial t^* = \dot{\alpha}c/U$, and non-dimensional plunge rate, $\overset{*}{h} = \partial(h/c)/\partial t^* = (\dot{h}/c)c/U$, as

$$\frac{U_{net}(t)}{U_{ref}} = \sqrt{\left[1 + \overset{*}{\alpha}(t) \left(\frac{1}{2} - \frac{x_p}{c}\right) \sin\alpha(t)\right]^2 + \left[\overset{*}{h}(t) - \overset{*}{\alpha}(t) \left(\frac{1}{2} - \frac{x_p}{c}\right) \cos\alpha(t)\right]^2}. \tag{6.3}$$

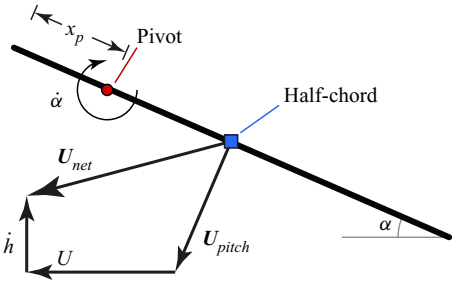

FIGURE 17. Contributions to half-chord velocity from the horizontal velocity ($U(t)$), plunge ($\dot{h}(t)$), and pitch (U_{pitch}).

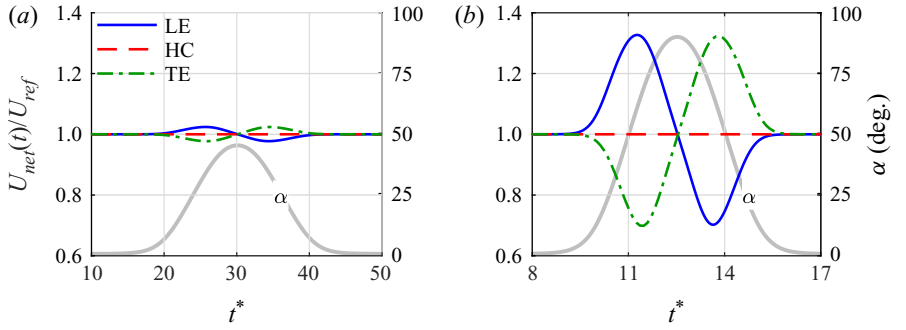

FIGURE 18. Plot of $U_{net}(t)/U_{ref}$ for the LE, HC and TE pivot cases at (*a*) $K = 0.05$ and (*b*) $K = 0.4$.

We note that this definition of U_{net} as the magnitude of the velocity of the half-chord point relative to the undisturbed fluid is an approximation. Relying on the QSTAT expression for A_0, it ignores the contributions of induced velocities due to shed vorticity. Furthermore, the choice of the half-chord point was made purely using the argument that pivoting about this location makes the QSTAT-calculated A_0 independent of pitch rate. Future work may result in a better estimate for U_{net} using advanced theories. The main aim in the current work, however, is to use a more representative velocity that, when used for calculating the leading-edge suction-force coefficient and LESP, will allow for proper comparison of unsteady aerofoils having different motion kinematics. It is worth mentioning that, when considering the QSTAT expression for the lift coefficient, C_l, instead of that for the A_0 term, the pitch-rate contribution becomes zero when the pivot is at the three-quarter-chord location. It is for this reason that the three-quarter-chord location is often considered as the 'neutral point' for calculating the effective angle of attack for pitch-rate effects. In the current work, however, the emphasis is on the leading-edge flow, which is governed by A_0 rather than by C_l. For this reason, the velocity of the half-point point is a more appropriate choice for defining the U_{net} in the current work for comparing leading-edge flows between motions.

Figure 18 shows the variations of $U_{net}(t)/U_{ref}$ with t^* for pitching motions about the leading edge, half chord and trailing edge for two example pitch rates: $K = 0.05$ and $K = 0.4$. For both the pitch rates, it is seen that $U_{net}(t)/U_{ref} = 1$ for the half-chord pivot cases, as expected. For the leading-edge cases, $U_{net}(t)/U_{ref} > 1$ during pitch-up and vice versa for the trailing-edge cases. For the leading-edge cases, the maximum $U_{net}(t)/U_{ref}$

is seen to be much smaller for the lower-K motion (approximately 1.03) than for the higher-K motion (approximately 1.33). These variations show the effect of K on the velocity correction for pivots that are not at the half-chord location.

Using this formulation of $U_{net}(t)/U_{ref}$, we present updated definitions for the leading-edge suction-force coefficient, pressure-coefficient and skin-friction coefficient distributions along the aerofoil arc length, s, and the LESP, using superscript 'net' to denote the use of the net-velocity magnitude for non-dimensionalization, as follows:

$$C_s^{net}(t) = \frac{C_s^{ref}(t)}{\left(U_{net}(t)/U_{ref}\right)^2}, \tag{6.4}$$

$$C_p^{net}(s/c, t) = \frac{C_p^{ref}(s/c, t)}{\left(U_{net}(t)/U_{ref}\right)^2}, \tag{6.5}$$

$$C_f^{net}(s/c, t) = \frac{C_f^{ref}(s/c, t)}{\left(U_{net}(t)/U_{ref}\right)^2}, \tag{6.6}$$

$$\mathcal{L}^{net}(t) = \frac{A_0(t)}{\left(U_{net}(t)/U_{ref}\right)} = \frac{\mathcal{L}^{ref}(t)}{\left(U_{net}(t)/U_{ref}\right)}. \tag{6.7}$$

We note that, for unsteady motions with constant forward velocity, zero plunge velocity and only pitching kinematics, if the pivot is at the half-chord location, U_{net} is always equal to U, and results in $C_s^{net}(t) = C_s^{ref}(t)$, $C_p^{net}(s/c, t) = C_p^{ref}(s/c, t)$ and $\mathcal{L}^{net}(t) = \mathcal{L}^{ref}$. For this reason, the results for C_s^{ref}, C_p^{ref}, C_f^{ref} and $\mathcal{L}^{ref}$ shown earlier in figures 7–13 are all valid with both the original and updated LESP formulations, as they are for pitching motions pivoted at the half-chord location.

7. Variation of the $\mathcal{L}^{net}$ at LEV initiation

This section presents the $\mathcal{L}^{net}$ values for the various cases, first for the low-Reynolds-number cases in § 7.1 and then for the high-Reynolds-number cases in § 7.2. The objective is to assess the effectiveness of the velocity correction used in the definition of $\mathcal{L}^{net}$. Additional detailed results of LESP vs t^* and U_{net}/U_{ref} vs t^* variations along with vorticity and velocity flow fields for NACA 0012 aerofoil for the medium- and high-K cases at the low and high Reynolds numbers for three pivot locations are presented in the appendix.

7.1. *Low-Reynolds-number cases*

Figures 19(a) and 19(b) show the variation of $\mathcal{L}^{net}$ with instantaneous $\mathrm{d}\alpha/\mathrm{d}t^*$ for the low-Re cases of the NACA 0012 and SD7003m aerofoils, respectively. It is seen that the results for the half-chord trend lines for $\mathcal{L}^{net}$ are identical to those presented earlier for $\mathcal{L}^{ref}$ in figure 15. This is to be expected, as $\mathcal{L}^{net}$ and $\mathcal{L}^{ref}$ are identical for pitching motions about the half-chord pivot location. In other words, the velocity correction used in the definition of $\mathcal{L}^{net}$ has not resulted in any improvement to the variation of LESP with pitch rate. Also seen is that the scatter in $\mathcal{L}^{net}$ relative to the trend lines is a little greater than that seen for $\mathcal{L}^{ref}$ in figure 15. In particular, for the SD7003m, the $\mathcal{L}^{net}$ values for the trailing-edge pivot cases for $K = 0.4$ and $K = 0.6$ and the three-quarter-chord pivot case for $K = 0.6$ are noticeably higher than the corresponding trend lines by approximately 0.05 to 0.15. These deviations in $\mathcal{L}^{net}$ for the three outliers are discussed in more detail in § 7.3, and can be

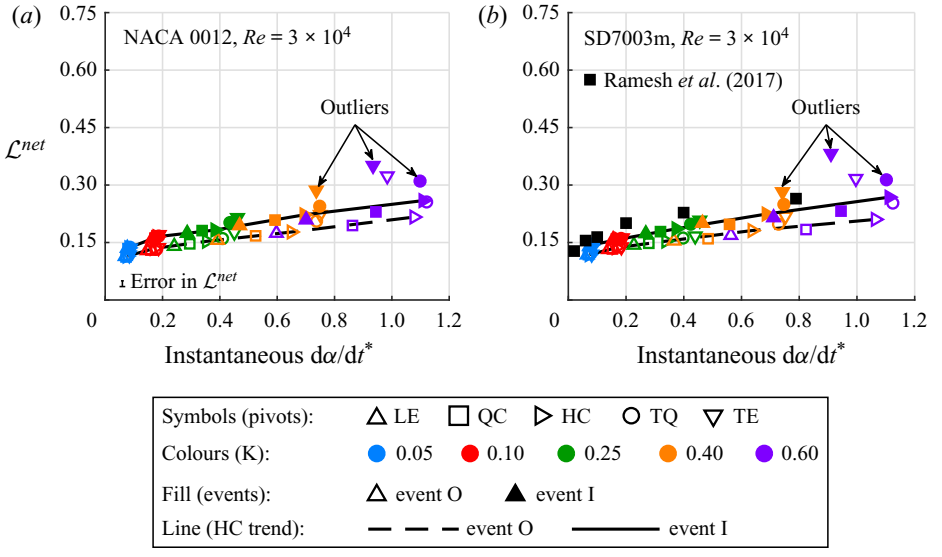

FIGURE 19. LEV initiation at low Reynolds numbers: variation of $\mathcal{L}^{net}$ at events O and I with instantaneous pitch rate for the (*a*) NACA 0012 and (*b*) SD7003 aerofoils at $Re = 30\,000$. Data points from Ramesh *et al.* (2017), converted to $\mathcal{L}^{net}$, are also included in (*b*).

traced to deviations for these cases in the flow behaviour at LEV formation. Ignoring these three outliers for both the aerofoils, the spread in the $\mathcal{L}^{net}$ values from the corresponding trend lines is close to the spread in $\mathcal{L}^{ref}$ from the trend lines in figure 15.

7.2. *High-Reynolds-number cases*

Figures 20(*a*) and 20(*b*) show the variation of $\mathcal{L}^{net}$ with instantaneous $\mathrm{d}\alpha/\mathrm{d}t^*$ for high-*Re* cases of the NACA 0012 and SD7003m aerofoils, respectively. Comparing against the $\mathcal{L}^{ref}$ variation in figure 16, we see that the velocity correction to the LESP has resulted in a dramatic improvement. The large scatter of $\mathcal{L}^{ref}$ values seen in figure 16 has instead been replaced by $\mathcal{L}^{net}$ values that fall in a small band around the two trend lines. This result demonstrates the importance of the velocity scaling used in the updated formulation of the $\mathcal{L}^{net}$.

It is interesting to note that, while the updated LESP formulation has resulted in substantially different results for the critical LESP for the high-*Re* cases, it has not resulted in significant change to the results for the low-*Re* cases. The reason for this difference can be understood by examining the detailed results presented in the appendix. It is seen that, although the time variation of U_{net}/U_{ref} for a given motion is independent of the Reynolds number, the value of U_{net}/U_{ref} at LEV initiation is very much dependent on the Reynolds number. For the high-*K* motions, LEV initiation occurs at much larger pitch angles at the higher Reynolds number than at the lower Reynolds number. Consequently, the value of U_{net}/U_{ref} at LEV initiation is close to the value of 1 for the low-Reynolds-number cases, causing $\mathcal{L}^{net}$ at LEV initiation to be close to the corresponding $\mathcal{L}^{ref}$. For the same motion at the higher Reynolds number, however, U_{net}/U_{ref} at LEV initiation is not close to the value of 1, causing the $\mathcal{L}^{net}$ at LEV initiation to be substantially different from the corresponding $\mathcal{L}^{ref}$.

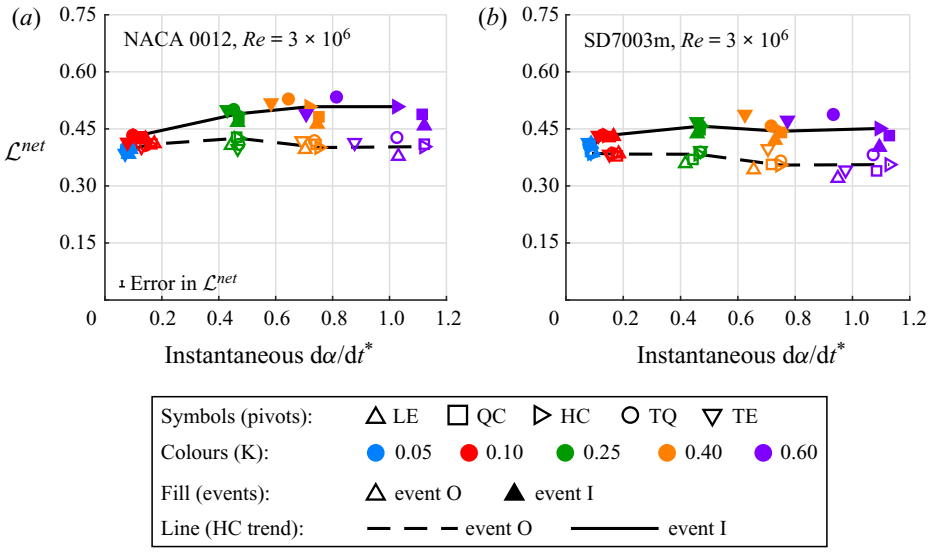

FIGURE 20. LEV initiation at high Reynolds numbers: variation of $\mathcal{L}^{net}$ at events O and I with instantaneous pitch rate for the (*a*) NACA 0012 and (*b*) SD7003m aerofoils at $Re = 3$ million.

7.3. *Discussion of the outliers*

Figure 21 compares the vorticity plots at event I for trailing-edge pivot cases of the SD7003m aerofoil for $K = 0.10$–0.60 for the low-Re cases on the top row and for the high-Re cases on the bottom row. For the low-Re cases, although theα values vary considerably with K for these cases, it is seen that the general flow pattern at the leading edge looks similar for $K = 0.10$ and 0.25. However, for the $K = 0.40$ and 0.60 cases, small, but noticeable, vortical structures are seen on the lower surface of the leading-edge region. For the high-Re cases, all the four cases including $K = 0.60$ have similar flow features. Although not shown, a similar vortical structure is also seen in the $K = 0.60$ three-quarter-chord pivot case for this aerofoil. This result shows that these three cases have leading-edge flows at LEV initiation that deviate from all the other low-Re LEV initiation cases for this aerofoil. It is for these three cases that the data points also form outliers in figure 19(*b*). This deviation is not seen in the high-Re case, and neither is there an outlier in the data points in figure 20(*b*). The reasons for these deviations are not clear and need further study. Nevertheless, the observation that the low-Re flow solutions for these three cases have deviations in the leading-edge flow behaviour at LEV initiation, and that these cases also show up as the outliers in the $\mathcal{L}^{net}$ scatter plot, but not in the $\mathcal{L}^{ref}$ scatter plot, provides support to the argument that the $\mathcal{L}^{net}$ is an improvement over the $\mathcal{L}^{ref}$ even for the low-Re cases.

For the NACA 0012 aerofoil, the leading-edge vortical structure that comprises the deviation from the flows for all the other low-Re cases is visible only for the $K = 0.6$ trailing-edge pivot case. However, as the data points for $K = 0.6$, three-quarter-chord pivot and $K = 0.4$, trailing-edge pivot cases deviate sufficiently from the trend lines in figure 19, that they are labelled as outliers.

8. Motion without LEV formation

In this section the variation of LESP is studied for a representative low-K motion that does not evince LEV formation. Figure 22 shows the vorticity and velocity-magnitude

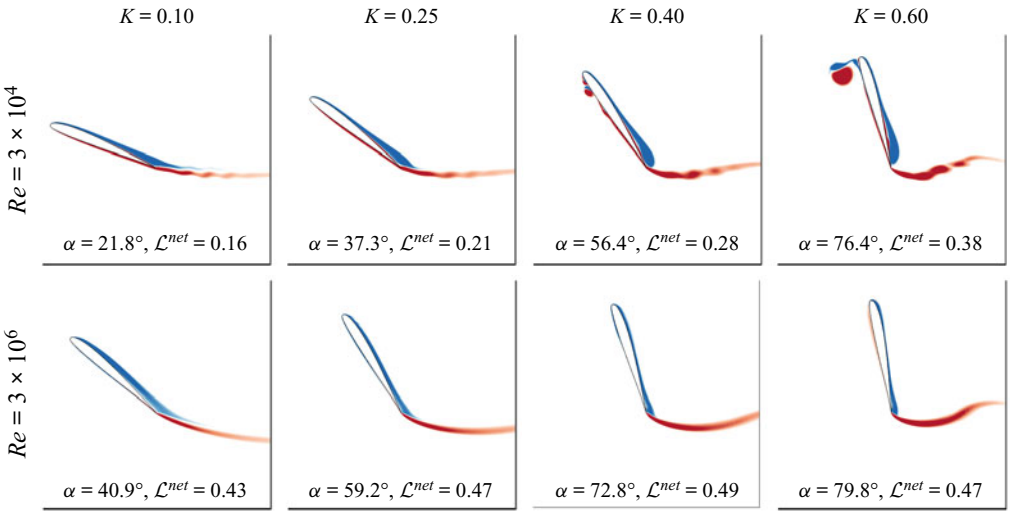

FIGURE 21. Flow features in the outliers: $\mathcal{L}$ and flow contours for the SD7003m aerofoil for the trailing-edge pivot cases and $K = 0.1$–0.6 for $Re = 30\,000$ (top row) and $Re = 3$ million (bottom row).

plots for the NACA 0012 aerofoil undergoing a pitch-up motion about the quarter-chord location with $K = 0.005$ at $Re = 3$ million. The flow images are shown for three time instants: (i) when the flow is fully attached, with $f = 1$, where f is the x/c location of the start of upper-surface boundary-layer separation; (ii) when $f = 0.5$; and (iii) at a pitch angle when the flow is fully detached, with $f = 0$. It is seen that, when the aerofoil pitches to a high angle, the flow becomes massively separated with no LEV formation. This behaviour is typical of low-K motions, of which steady flow ($K = 0$) is a subset. Figure 23 shows the variation of inviscid and viscous LESP with t^* for this motion. Also marked in this plot are the t^* values corresponding to the three time instants depicted in figure 22. It is seen that the maximum viscous LESP in this case is 0.31, which is less than the lowest LESP value of 0.39 seen in the curves in figure 20(*a*). This representative example confirms that, for a motion for which the LESP never exceeds $\mathcal{L}^{net}_{crit}$, no LEV formation occurs. Instead such motions evince massively separated flows.

9. Post-leading-edge-separation behaviour of LESP

As discussed in § 2.3, based on the understanding and knowledge available then, the LDVM low-order model (Ramesh *et al.* 2014) assumed that after initiation of LEV formation, the LESP remains constant until termination of the LEV formation. This assumption worked well for the low-Re cases used in that work. One of the objectives of the current work, in which the LESP is calculated from RANS CFD solutions, was to study the behaviour of leading-edge suction after LEV initiation, and to improve the low-order model based on the understanding gained. With this aim, this section presents the results for the LESP behaviour after flow separation from the leading edge in cases with and without LEV formation.

To understand the behaviour of the LESP, it is useful to recall how the suction force is generated. Consider an aerofoil with attached flow at the leading edge, at a positive angle of attack, as illustrated in figure 24. The stagnation point is located on the lower surface. The upper-surface flow travels from the stagnation point towards the

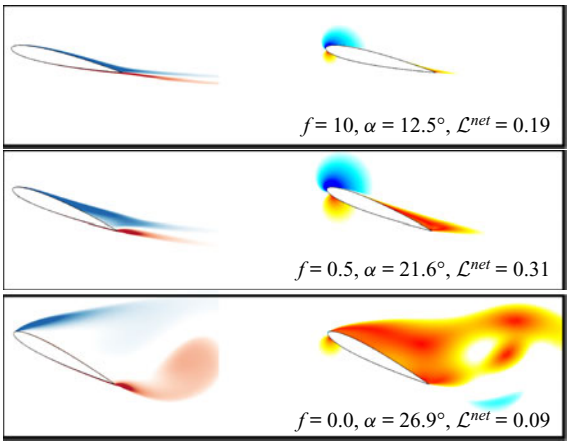

FIGURE 22. Vorticity (left) and velocity-magnitude (right) plots for the NACA 0012 aerofoil ($Re = 3$ million, $K = 0.005$) for a case with no LEV.

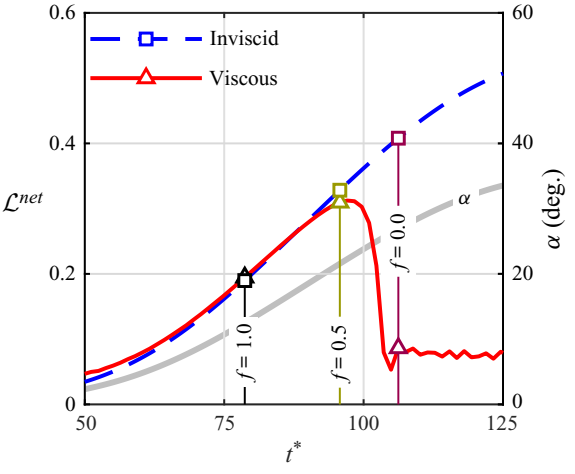

FIGURE 23. Variation of LESP with t^* for the low-K motion ($K = 0.005$) of the NACA 0012 aerofoil at $Re = 3$ million.

leading edge and turns around the leading edge before flowing over the upper surface. This flow curvature (κ) at the leading edge is associated with a low pressure region which exerts a forward 'suction force' on the aerofoil. In analysing the behaviour of the suction force as the leading-edge flow undergoes separation, we use the variation of this outer-streamline curvature at the leading edge to provide an explanation for the leading-edge suction behaviour. The outer-streamline curvature is estimated from the CFD results by considering three points on a streamline just outside the boundary layer or shear layer near the leading edge (shown in figure 24) to calculate the curvature.

The following sections are organised as follows. In § 9.1 we first present results for cases with LEV formation and then in § 9.2 we present the low-K cases for which the aerofoil stalls without LEV formation for the NACA 0012 aerofoil. Then § 9.3 draws parallels between the LESP trends observed for the cambered SD7003m aerofoil with those for the symmetric NACA 0012 aerofoil for the range of motions and Reynolds

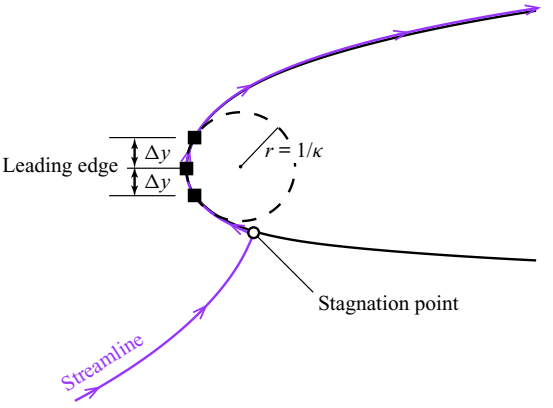

FIGURE 24. Representation of the flow streamline curvature around the leading edge.

numbers covered in this work. To illustrate the importance of correctly modelling the post-separation behaviour of LESP, § 9.4 presents an example result from a low-order calculation of LEV shedding using the new insight gained from the current work. Finally, § 9.5 presents the trends in the slope of the LESP drop after leading-edge separation for all cases simulated in this work to guide future efforts in modelling the LESP in low-order methods.

9.1. *Cases with LEV formation*

Figures 25(*a*) and 25(*b*) show the variation with t^* of inviscid and viscous LESP, and streamline curvature, κ, respectively, for a NACA 0012 aerofoil at a Reynolds number of 3 million, pitching at $K = 0.4$, for the period of time starting from just prior to the initiation of LEV formation to the termination of LEV formation. On these plots are marked eight points corresponding to a sequence of events. The vorticity contours and streamline plots for these eight time instants are shown in figure 26. From these two figures we see that at event (*a*) the viscous LESP is nearly equal to the inviscid value because the leading-edge flow is attached and the curvature is at a high value. At (*b*) and (*c*) we see the early stages of an LEV being formed, resulting in the progressive deviation of the viscous LESP from the inviscid curve, and the beginnings of a sharp drop in streamline curvature at the leading edge. At points (*d*), (*e*) and (*f*) there is a shear layer at the leading edge that feeds a growing LEV structure. As a result of the flow separation at the leading edge, the streamline curvature is close to zero, and the viscous LESP values have large deviations from the corresponding inviscid values. By the time instants corresponding to points (*g*) and (*h*), the pitch angle of the aerofoil has started to decrease, resulting in the beginning of the termination process for the LEV. From the flow images (figure 26), it is seen that the streamline curvature has started to increase, which is also reflected in the κ variation and in the decreasing difference between the inviscid and viscous LESP values (figure 25*a*). This example shows that (i) soon after LEV initiation, there is a drop in LESP, and (ii) the reason for this drop is that the separation of the leading-edge flow results in a loss in streamline curvature for the leading-edge flow.

Similar inferences regarding the suction behaviour post-LEV initiation can be made for the NACA 0012 aerofoil undergoing a high-K motion with LEV shedding at a low-Re by observing the trends in LESP and κ from figure 27, and the vorticity contours and streamline plots from figure 28 for six time instants. Event (*a*) shows attached flow at the

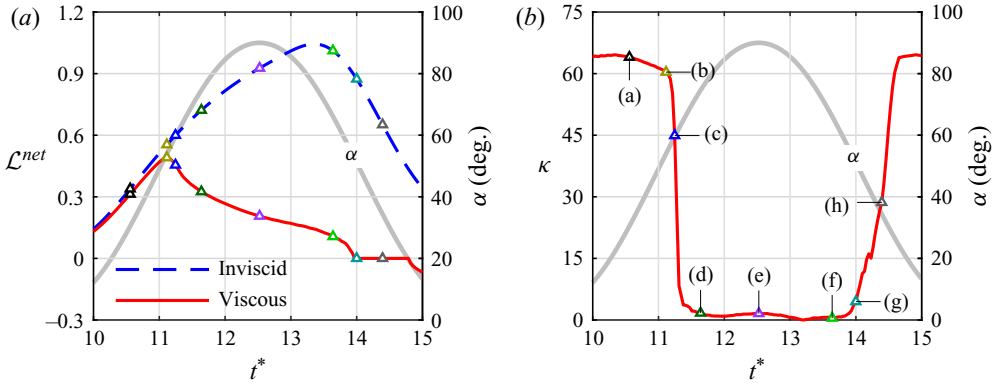

FIGURE 25. Variation of LESP and curvature with t^* for the NACA 0012 aerofoil at $Re = 3$ million, $K = 0.4$, and pivoted at the quarter chord.

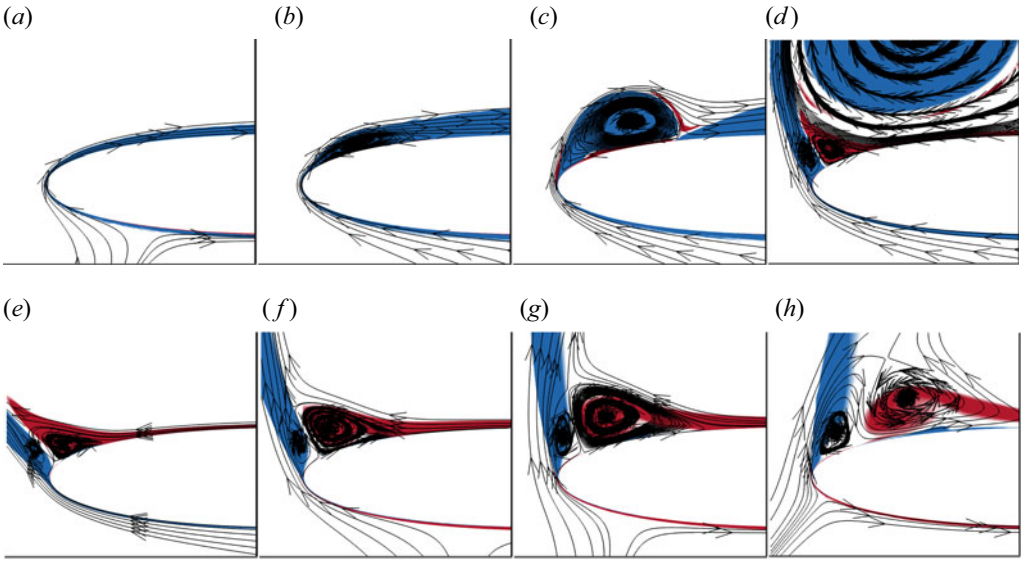

FIGURE 26. Vorticity and streamline plots for the leading-edge region at eight time instants corresponding to figure 25.

leading edge, negligible difference between viscous LESP from inviscid predictions and a high curvature value. As the LEV starts to initiate at event (*b*), the deviation between viscous and inviscid LESP starts to increase and a gradual drop in curvature is observed. As the LEV grows (event (*c*)), figure 27(*b*) displays a sharp drop in curvature, with the low value being maintained as the shear layer continues to feed into the LEV structure (event (*d*)). Correspondingly, figure 27(*a*) shows an increasing difference between inviscid and viscous LESP as the motion progresses from event (*c*) to (*d*). As LEV shedding starts to terminate (event (*e*)) and flow starts to reattach at the leading edge (event (*f*)), the deviation of viscous LESP from inviscid behaviour reduces and the curvature increases. Overall, this example confirms the correlation between leading-edge suction and streamline curvature, even for the low-*Re* cases.

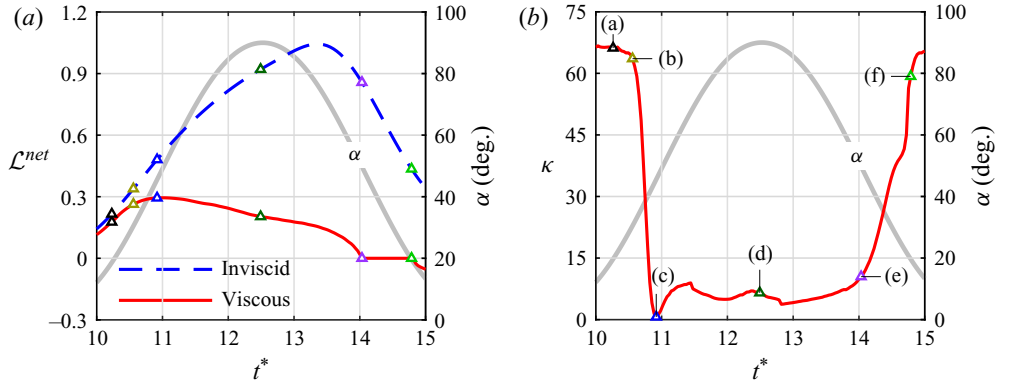

FIGURE 27. Variation of LESP and curvature with t^* for the NACA 0012 aerofoil at $Re = 30\,000$, $K = 0.4$, and pivoted at the quarter chord.

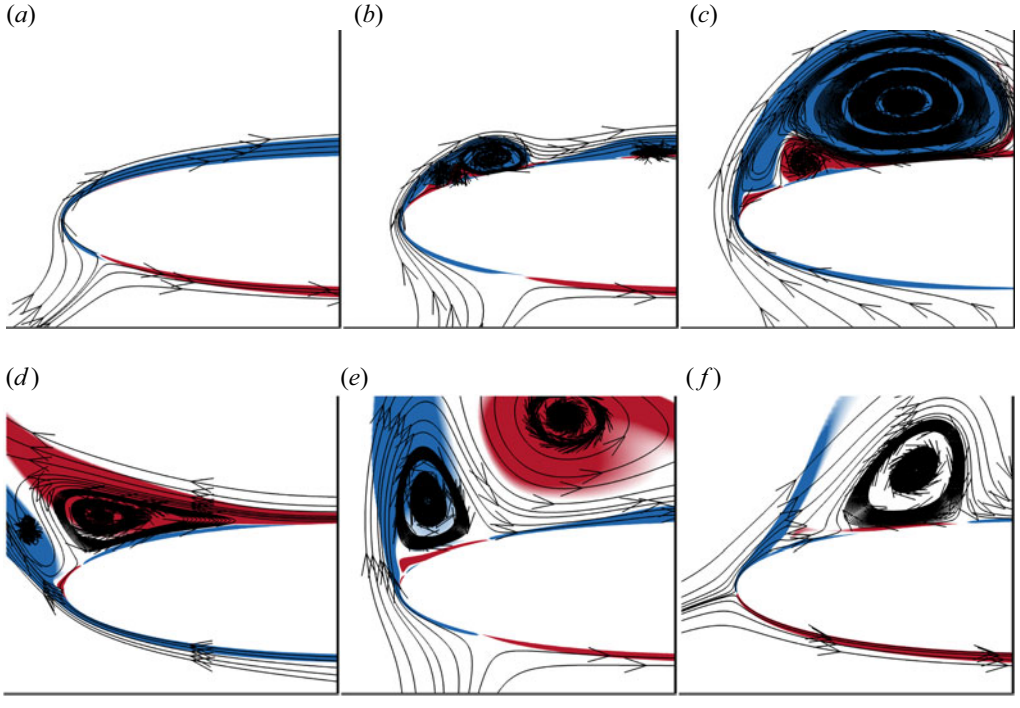

FIGURE 28. Vorticity and streamline plots for the leading-edge region at the six time instants corresponding to figure 27.

9.2. *Cases without LEV formation*

For low pitch-rate cases (of which steady flow ($K = 0$) is a subset) in which LEV shedding does not occur, a drop in LESP similar to that observed for the high-K case in § 9.1 occurs when flow separation reaches the vicinity of the leading edge. Figure 29 shows the variation of (*a*) inviscid and viscous LESP and (*b*) leading-edge flow curvature (κ) for a NACA 0012 aerofoil undergoing a low-K motion. Each row in figure 30 shows the velocity-magnitude contour around the aerofoil, vorticity around the leading-edge region

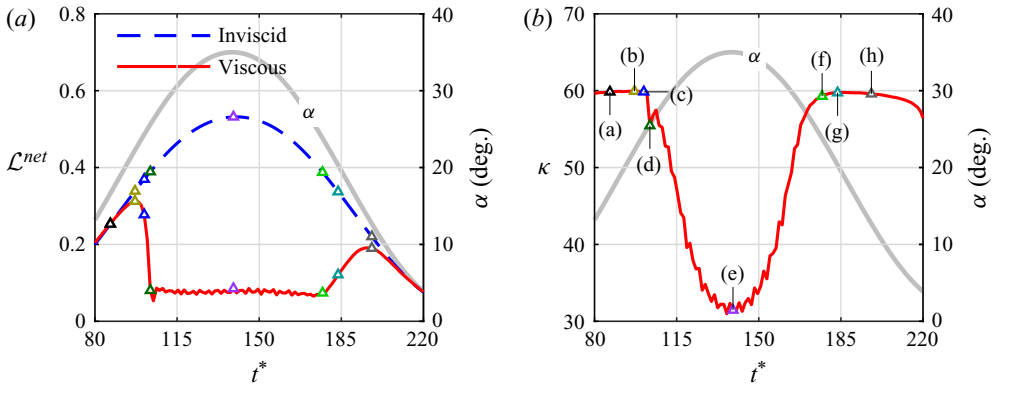

FIGURE 29. Variation of LESP and curvature for a low pitch-rate simulation without LEV formation (NACA 0012, $Re = 3 \times 10^6$, $K = 0.005$, $0^\circ - 35^\circ - 0^\circ$ pitch-up-return, quarter-chord pivot).

up to $x/c = 0.25$, the upper surface-C_f^{net} at the leading edge and the C_p^{net} vs y/c variation up to the quarter chord for the eight time instances marked in figure 29(*b*). Figures 29 and 30 show that, at events (*a*) and (*b*), where there is boundary-layer separation on the aft portion of the upper surface but flow at the leading edge is attached, the difference between inviscid and viscous LESP is negligible and the curvature is high and constant. At event (*c*), as flow starts to separate at the leading edge, viscous LESP starts to deviate from inviscid behaviour and curvature starts to decrease. Further increase in the angle of attack (event (*d*)) results in increased deviation of the viscous LESP from inviscid predictions and a corresponding decrease in curvature. At event (*e*), when the angle of attack is maximum and the degree of flow separation is at its highest for the motion, the deviation in LESP reaches a peak value and the curvature is close to zero and is at its minimum. As the aerofoil pitches down and the angle of attack decreases (events (*f*) and (*g*)), a favourable pressure gradient is re-established on the upper surface, leading to flow reattachment at the leading edge. A corresponding decrease in the difference between inviscid and viscous LESP and an increase in flow curvature is observed. Once flow fully reattaches at the leading edge at event (*h*), viscous LESP reaches a local maximum and proceeds to return to inviscid behaviour with the flow curvature once again reaching its maximum value. Observations from the current low-K case correspond well with the high-K example discussed in § 9.1 in that, similar to cases where LEV shedding occurs, leading-edge flow separation also causes a loss in streamline curvature, which in turn leads to a drop in leading-edge suction. It is noted that, in these cases where there is no LEV formation, the LEV signatures of inflection in the surface-C_f^{net} and the surface-C_p^{net} distributions are also not present, confirming that the absence of those signatures are reliable indicators of the absence of LEV formation.

9.3. *Post-leading-edge-separation LESP behaviour for the SD7003m aerofoil*

Figure 31 shows the time histories of the LESP for the SD7003m aerofoil undergoing (*a*) a high-K motion with LEV shedding and (*b*) a low-K motion without LEV shedding for both low- and high-Re cases.

As seen with the NACA 0012 aerofoil, the viscous LESP shows a more gradual deviation from inviscid behaviour upon LEV initiation for the low-Re case as compared with the

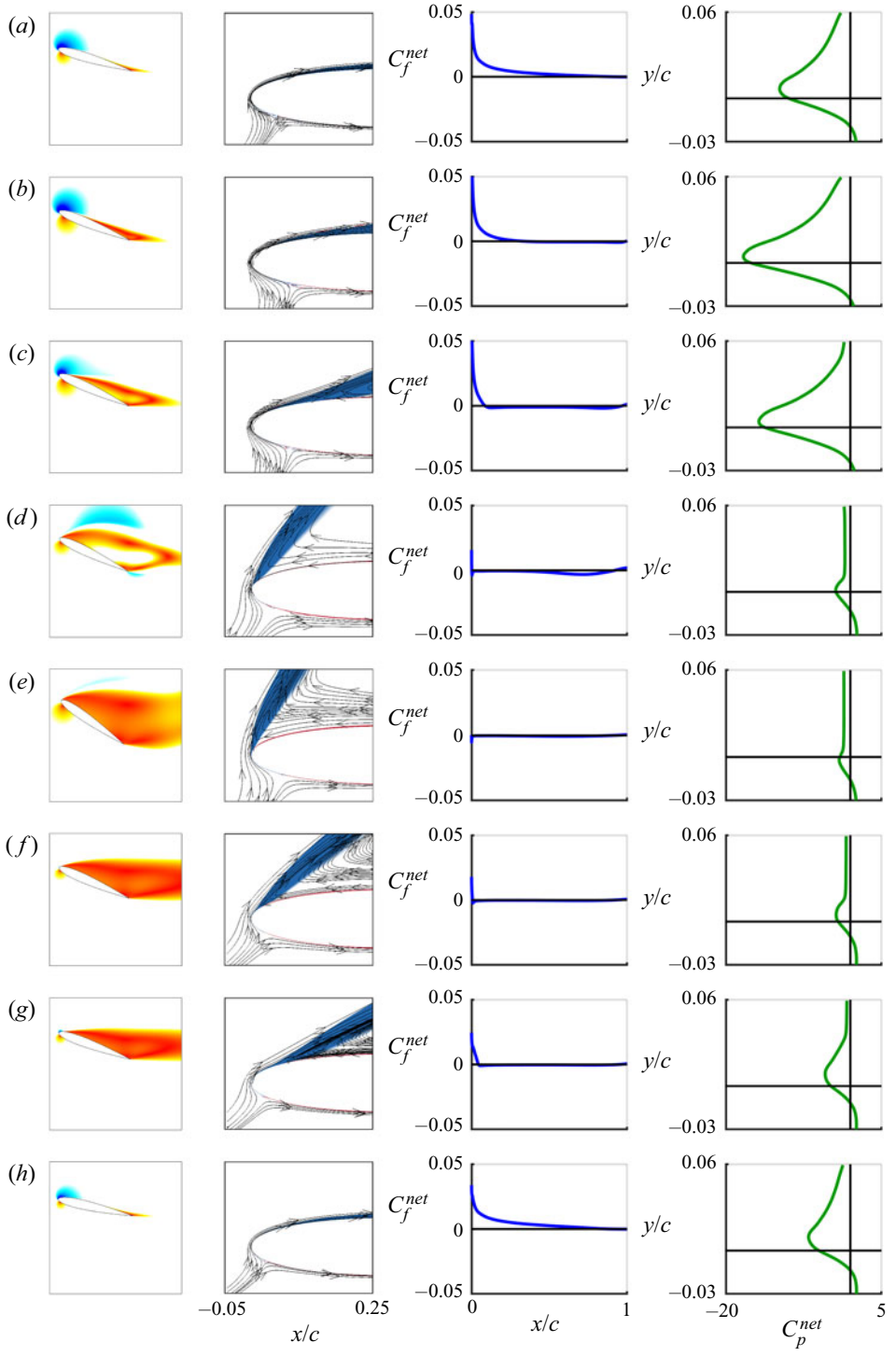

FIGURE 30. Velocity magnitude, vorticity, skin friction and pressure plots at the eight time instants in figure 29 for the low pitch-rate simulation without LEV (NACA 0012, $Re = 3 \times 10^6$, $K = 0.005$, 0°–35°–0° pitch-up-return, quarter-chord pivot).

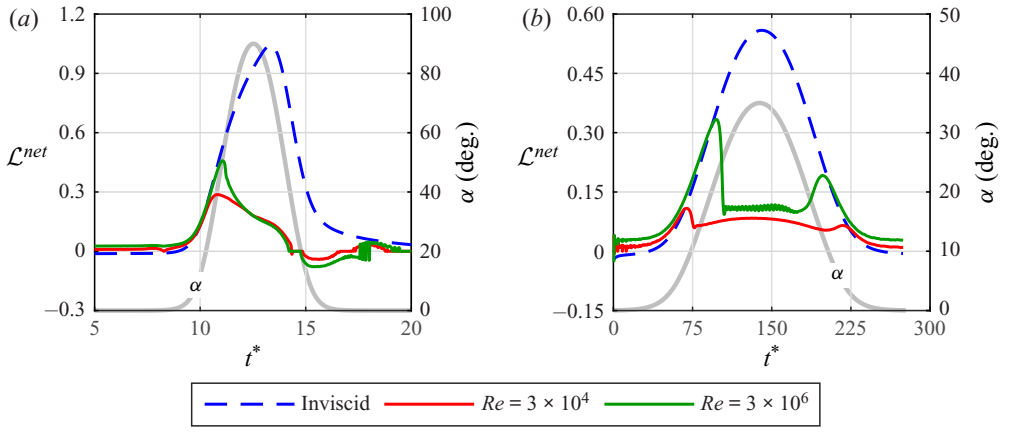

FIGURE 31. Post-separation LESP trends for the SD7003m aerofoil: (*a*) high-K motion and (*b*) low-K motion.

high-Re case for the high-K motion (figure 31*a*). For the low-K motion without LEV shedding (figure 31*b*), the peak LESP does not exceed the $\mathcal{L}^{net}_{crit}$ values of 0.14 and 0.41 (from figures 19*b* and 20*b*) for the low- and high-Re cases, respectively, reaffirming the hypothesis that no LEV formation occurs when LESP does not exceed $\mathcal{L}^{net}_{crit}$ for the given aerofoil and Reynolds number. Additionally, the behaviour of the LESP after leading-edge separation for the different motions of the SD7003m aerofoil is similar to that observed for equivalent motions of the NACA 0012 aerofoil at both Reynolds numbers.

9.4. *Effect of the LESP drop on low-order modelling accuracy*

To illustrate the importance of the insight gained here on the drop in LESP after LEV initiation, an example high-Reynolds-number and high-K motion of the SD7003m aerofoil is analysed using a version of the LDVM code (Ramesh *et al.* 2014) with the original and modified implementations of the post-LEV behaviour of the LESP. The results from these low-order implementations are compared with the computational results for this case in figure 32. In the original implementation, labelled LOM1, the LESP is maintained at a constant value of $\mathcal{L}^{net}_{crit}$ during LEV shedding. In the modified implementation, labelled LOM2, the LESP drops linearly from LESP_{crit} at LEV initiation to zero using a $\mathrm{d}(\mathcal{L}^{net})/\mathrm{d}t^*$ slope that is close to the slope seen in the CFD result. Figure 32(*a*) compares the LESP variations from the CFD and the two low-order implementations. Figure 32(*b*) compares the low-order discrete-vortex plot from LOM1 with the vorticity distribution from CFD, showing that the original low-order implementation results in an inaccurate prediction of the location of the LEV structure. With the drop in LESP modelled, as seen in figure 32(*c*), the location of the LEV structure predicted by the modified low-order method (LOM2) agrees well with that seen in the CFD result. Although the $\mathrm{d}(\mathcal{L}^{net})/\mathrm{d}t^*$ used in LOM2 was obtained from the CFD result, this example nevertheless illustrates the importance of correctly modelling the post-separation behaviour of LESP, especially for the high-Reynolds-number cases in which the critical LESP is high (usually > 0.4), resulting in a significant drop. On the other hand, for low-Reynolds-number cases, because the critical LESP is quite low ($\approx$0.25 or less), not modelling the small drop did not affect the accuracy of the low-order model noticeably. It is because of this reason that

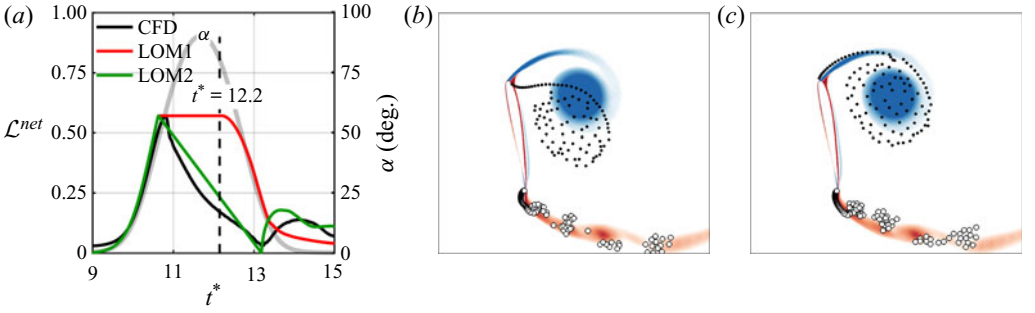

FIGURE 32. Effect of modelling the post-separation LESP drop on low-order results for the SD7003m aerofoil at $Re = 3 \times 10^6$, pitching about the quarter chord at $K = 0.6$: (*a*) LESP variations from CFD, original model (LOM1) and modified model (LOM2); (*b*) discrete-vortex plot from LOM1 compared with the vorticity plot from CFD at $t^* = 12.2$; and (*c*) discrete-vortex plot from LOM2 compared with the vorticity plot from CFD.

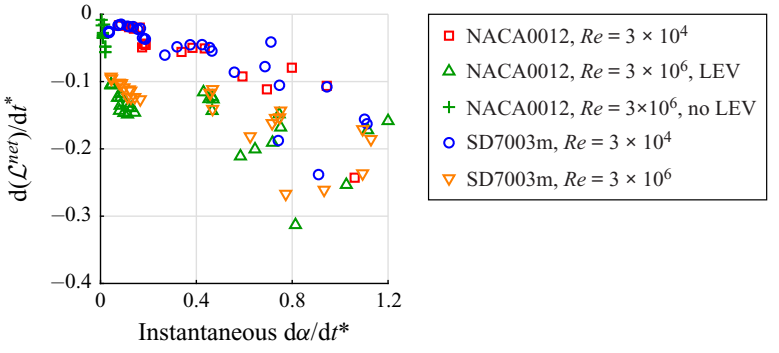

FIGURE 33. Scatter plot of $d(\mathcal{L}^{net})/dt^*$ after leading-edge separation for all cases.

the results in Ramesh *et al.* (2014) (all low-Reynolds-number cases) agreed well with the experimental and CFD results even with the original implementation of the post-separation LESP behaviour.

9.5. *Rate of LESP drop after leading-edge separation*

As demonstrated in § 9.4, in order to accurately model the LESP behaviour in low-order methods, the data on the rate of LESP drop is useful. The compiled post-leading-edge-separation $d(\mathcal{L}^{net})/dt^*$ data for all the cases simulated in the current work (table 1) have been plotted against instantaneous $d\alpha/dt^*$ in figure 33. The instantaneous $d\alpha/dt^*$ used for the data corresponds to the value at initiation of LEV formation (for cases in which the stall was the result of LEV formation) or the value at which separation reached the leading edge (for cases in which stall occurred without LEV formation). For the symmetric NACA 0012 and cambered SD7003m aerofoils at Reynolds numbers 30 000 and 3 million, the $d(\mathcal{L}^{net})/dt^*$ ranges from -0.25 to -0.008 for various motion kinematics. This information can be used in future research to develop extensions of LDVM-like low-order methods (Ramesh *et al.* 2014; Hirato *et al.* 2019; Narsipur *et al.* 2019) in which the post-separation LESP drop is modelled without the need to acquire it from a CFD solution of that problem. An early version of such a low-order method is described in Narsipur (2017) and Narsipur, Gopalarathnam & Edwards (2018).

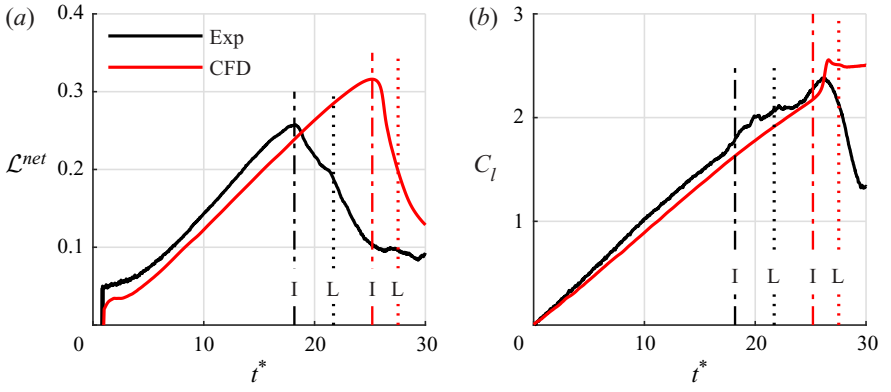

FIGURE 34. Comparison of CFD predictions with the experimental results of Gupta & Ansell (2019) for a NACA 0012 aerofoil undergoing a constant pitch-up motion about the quarter chord with $k = 0.05$ and $Re = 0.50 \times 10^6$: (*a*) LESP vs t^* and (*b*) C_l vs t^*.

9.6. *Verification of trends in leading-edge suction with experimental data*

All the data and resulting analysis presented in the above sections are based on computational results. It is therefore prudent to verify the trends observed in LESP behaviour with experimental data.

Figure 34 compares CFD results with experimental data from Gupta & Ansell (2019) for a NACA 0012 aerofoil undergoing a constant pitch-up motion about the quarter chord at a Reynolds number of 500 000. The LESP and C_l predictions from CFD simulations are compared with experimental data in figures 34(*a*) and 34(*b*), respectively. Figure 35 compares the vorticity contour data from CFD simulations with the vorticity fields from time-averaged particle image velocimetry measurements from the experiment at the instant of LEV initiation (event I) and at a point where the LEV is well formed (event L). As explained in § 3.4, the inflection in the C_p^{net} could be used to identify the point of LEV initiation (event I). However, due to the sparsity of pressure ports at the leading edge in the experimental investigation, the C_p^{net} distributions could not be reliably used to identify event I. For the current case, the experimental vorticity field data was used to identify event I.

It is seen that the LESP measurements from the experiment before LEV initiation are higher when compared with CFD predictions. Experimental vorticity measurements (figure 35) indicate the first sign of an LEV at $\alpha = 18.2^\circ$ while the signature of event I from the CFD solution was found to occur at a higher angle of attack ($\alpha = 25.2^\circ$). After LEV initiation, both CFD and experimental results show a drop in the suction force and a continuous decrease as the LEV grows.

Lift results from the computations compare well with experimental measurements (figure 34*b*). Both experimental and computational C_l show a linear increase in lift until the point of LEV initiation, after which both methods show a nonlinear rise in lift. Overall, while CFD predicts LEV initiation at a higher angle of attack, trends in LESP, lift and vorticity flow fields compare very well with experimental measurements.

Next we consider experimental results for an S801 aerofoil undergoing a sinusoidal pitching motion ($\alpha_{mean} = 14^\circ$, $\alpha_{amplitude} = 10^\circ$) about the quarter chord with $k = 0.107$ at a Reynolds number of 750 000 from wind tunnel experiments conducted by Ramsay, Gregorek & Hoffmann (1996). Figure 36 shows (*a*) the leading edge C_p^{net} vs y/c data

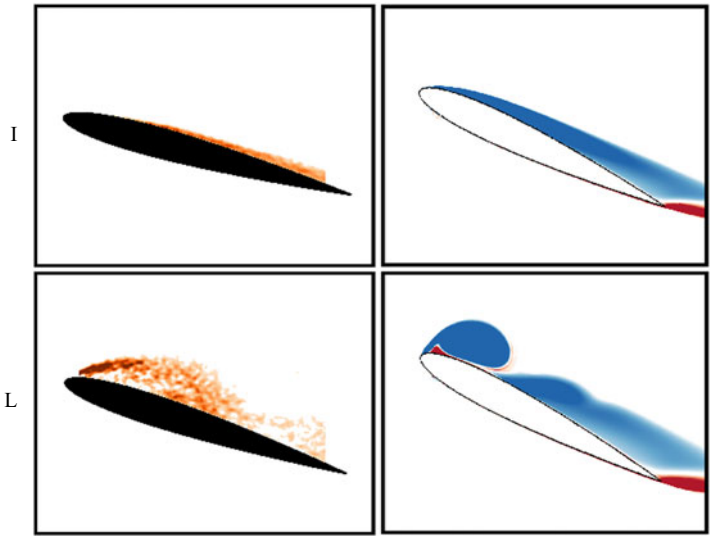

FIGURE 35. Flow visualization data at events I and L from experiments (left) and CFD (right) for a NACA 0012 aerofoil undergoing a constant pitch-up motion about the quarter chord with $k = 0.05$ and $Re = 0.50 \times 10^6$.

for three frames centred about event I, (*b*) the C_l variation and (*c*) the $\mathcal{L}^{net}$ variation for this case. The availability of a fine distribution of leading-edge pressure data helped in accurately identifying the time instant of event I at $t^* = 4.44$ from the inflection in the C_p^{net} vs y/c data (shown in figure 36*a*). The inset in figure 36(*a*) shows the evolution of the inflection in C_p^{net} at event I by plotting the C_p^{net} vs y/c distribution at time instants immediately before and after said event. An error of $\Delta t^* = 0.74$ is assumed due to the discrete time steps at which the experimental pressure data is available. An additional confirmation of LEV initiation and development is available from figure 36(*b*) at the point where a nonlinear increase in C_l occurs during the aerofoil's upstroke, a behaviour typically attributed to LEV formation (Leishman 2002), which in the current case lies within the error bounds of the time instant at which the leading edge C_p^{net} distribution indicates event I. At and following event I, figure 36(*c*) shows a drop in LESP as the LEV initiates and develops, thereby confirming the trends observed in the numerical simulations.

In other experimental investigations, Deparday & Mulleners (2019) and Ansell & Mulleners (2020) estimated the LESP from surface pressure and time-resolved particle image velocimetry measurements of a sinusoidally pitching OA209 aerofoil ($\alpha = 20^\circ \pm 8^\circ$, $k = 0.05$, quarter-chord pivot) at a Reynolds number of 920 000. The trends from their work are similar to those seen in the current work, providing further experimental confirmation for the observations made in the current work.

10. Conclusions

A large set of computational results from unsteady RANS simulations of pitching aerofoils in incompressible flow, supplemented with a few experimental results from the literature, were studied to examine the behaviour of the LESP before, during and after flow separation from the leading edge, both in cases with LEV formation and in

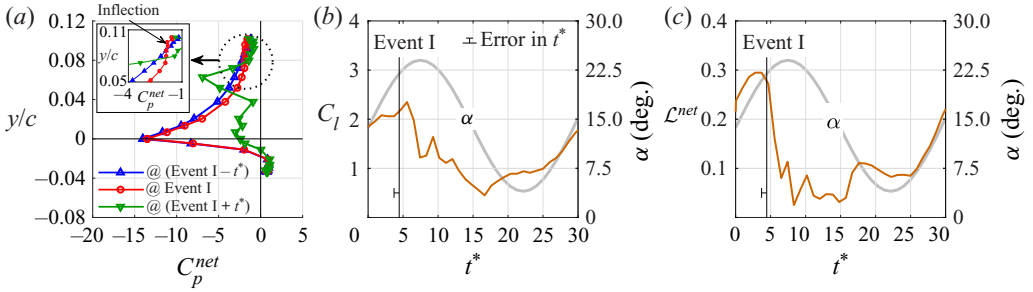

FIGURE 36. Experimental data for an S801 aerofoil undergoing a sinusoidal pitch motion of $14^\circ \pm 10^\circ$ about the quarter chord with $k = 0.107$ and $Re = 0.75 \times 10^6$ (Ramsay *et al.* 1996): (*a*) C_p^{net} vs y/c, (*b*) C_l vs t^* and (*c*) $\mathcal{L}^{net}$ vs t^*.

cases in which there is no LEV formation. Effects of aerofoil shape, Reynolds number, pivot location and non-dimensional pitch rate on the LESP behaviour were quantified. The instantaneous LESP for any case was extracted from the computational results by integrating the instantaneous pressure distribution on the leading-edge portion of the aerofoil, and this value was shown to match with the theoretical LESP for attached-flow conditions. When flow separation is present, the CFD-derived 'viscous LESP' value takes into consideration the viscous effects and, hence, deviates from the theoretical 'inviscid LESP' value. It is this capability to extract the viscous LESP from CFD that provided the ability to study the LESP behaviour even after leading-edge separation.

For all cases with LEV formation, the time instant for the initiation of LEV formation could be reliably identified from inflections in the surface C_f and C_p distributions near the leading edge. Conversely, for all cases without LEV formation, these signatures were absent. For the former set of cases, the LESP values at LEV initiation, or critical LESP, for a given aerofoil at a low Reynolds number of 30 000 were found to be independent of pivot location and had a small dependence on the instantaneous pitch rate. These trends agree with those in recent literature. For a high Reynolds number of 3 million, although the variation with pitch rate was similar to that seen for the low-*Re* case, a considerable scatter in the critical LESP was seen due to variation in the pivot location at high pitch rates. A careful study of the problem led to the realization that, at high motion rates, the net velocity of the aerofoil relative to the undisturbed fluid varies considerably with time during the motion, and it is significantly different from the constant reference velocity typically used for non-dimensionalizing pressures, forces and LESP. Using an expression derived from theory for the ratio of the net velocity to the forward velocity, an updated LESP formulation was developed. With this updated LESP, the scatter due to the effect of pivot location on the high-*Re* critical LESP values for LEV initiation is dramatically reduced, leaving only the small variation of critical LESP with pitch rate. For the low-*Re* cases, the updated LESP formulation did not change the results for LEV initiation appreciably except for cases with high pitch rates and aft pivot locations, which form outliers in the data. It was shown that these outliers also had leading-edge flow features not present in the other cases. The reasons for these deviations are not clear and need further study. Nevertheless, this correlation between the deviation in the leading-edge flow from that for other cases and the deviation in the updated-formulation critical LESP values from expected trends provides support for the validity of the updated LESP formulation. In earlier work, the small increase in critical LESP with increase in pitch rate was attributed to the fact that the inviscid LESP does not take into consideration the effect of trailing-edge

flow separation, which is increasingly present as the pitch rate reduces. The current work, however, shows that this trend is present even in the CFD-derived viscous LESP values, leading to the conclusion that a decreasing amount of trailing-edge flow separation alone does not explain the increase in critical LESP with pitch rate. For any given aerofoil, the critical LESP was seen to increase with Reynolds number. This behaviour is to be expected, as the predicted level of boundary-layer separation at higher Reynolds numbers is typically delayed compared with lower Reynolds numbers due to the energizing effects of modelled turbulence.

At low pitch rates, the aerodynamic behaviour is characterized by boundary-layer flow separation moving from the trailing edge towards the leading edge, resulting in massive separation with no LEV formation. For these cases, the peak LESP value was seen to be less than the critical LESP for LEV initiation, demonstrating that the LESP reaching the critical value is necessary for formation of the LEV. Irrespective of whether or not an LEV formed, soon after leading-edge flow separation, the LESP was seen to drop sharply to a value close to zero. By estimating the curvature of the outer-flow streamline at the leading edge, it is shown that this decrease in LESP is correlated with the decrease in streamline curvature due to the leading-edge flow separation. More specifically, the deviation of the viscous LESP from the inviscid value is seen to be well correlated with the loss in streamline curvature due to leading-edge flow separation. When the leading-edge flow reattaches due to a reduction in the pitch angle during the downstroke, the leading-edge streamline curvature increases again, and the viscous LESP again becomes close to the inviscid value. The observation that the LESP drops after leading-edge separation is an important finding because it can be used to improve the accuracy of low-order models for unsteady aerofoils with LEV shedding.

While the LESP behaviours determined using the results of unsteady RANS simulations are in agreement with those determined from experiments, future work could focus on verification of these results using high-fidelity CFD methods like large-eddy simulations. Three interesting research questions that could form the focus of a future investigation are as follows. (i) What is the fundamental reason for the variation in critical LESP with aerofoil shape and Reynolds number? (ii) What is the reason for the small, but nevertheless noticeable, change in critical LESP with non-dimensional pitch rate? (iii) What factors affect the rate of decrease in LESP after leading-edge separation? Addressing these questions would help further advance our understanding of leading-edge flows and improve our ability to model aerofoil stall.

The surface data from CFD and time histories of the inviscid and viscous forces and LESP for all 115 motions presented in this paper have been provided in the supplementary material at https://doi.org/10.1017/jfm.2020.467.

Acknowledgements

The authors wish to gratefully acknowledge the support of the U.S. Army Research Office through grant W911NF-13-1-0061, monitored by Dr Matthew Munson. Professor Phillip Ansell of the University of Illinois at Urbana-Champaign is thanked for sharing the experimental data (Gupta & Ansell 2019) used in this paper. Helpful discussions with Dr Kiran Ramesh of the University of Glasgow are also acknowledged.

Declaration of interests

The authors report no conflict of interest.

Supplementary material

Supplementary material are available at https://doi.org/10.1017/jfm.2020.467.

Appendix. Detailed LESP and flow results for LEV initiation

This appendix presents detailed results for the NACA 0012 aerofoil at two Reynolds numbers, $Re = 30\,000$ and 3 million, in figures 37 and 38, respectively. In each of the figures, subfigure (a) presents the results for the medium pitch-rate motions ($K = 0.05$) and subfigure (b) for the high pitch-rate motions ($K = 0.4$). The results are co-plotted for three pivot locations for each subfigure: leading edge (LE), half-chord (HC), and trailing edge (TE). In each case, the plots focus only on the t^* from shortly before LEV initiation to shortly after LEV formation. For each pitch rate (each subfigure), the top row shows the variation of inviscid and viscous $\mathcal{L}^{ref}$ with t^* for the three pivot locations, with the time instants of event I marked for each. The next row shows the time variation of U_{net}/U_{ref}, with the time instants for event I (LEV initiation) marked for each pivot location. The third row presents the time variations of the inviscid and viscous $\mathcal{L}^{net}$ for the three pivot locations. The last three rows present vorticity and velocity-magnitude plots at event I for the leading-edge, half-chord, and trailing-edge pivots, respectively.

Examining the results for the low-Re, medium-K cases in figure 37(a) first, we see that U_{net}/U_{ref} does not deviate much from the value of 1 at any time during the motion, because of which there is no noticeable difference between the time variations of the $\mathcal{L}^{ref}$ and the $\mathcal{L}^{net}$ curves. The three flow-field subfigures show that, although there is an increase in pitch angle for event I from 11.5 to 16.2 degrees with change in the pivot location from leading edge to trailing edge, the LESP values are the same.

When examining the results for the low-Re, high-K cases in figure 37(b) next, we see that the U_{net}/U_{ref} curves for the leading- and trailing-edge cases have maximum deviations of ± 0.3 from the value of 1. As a result, the $\mathcal{L}^{net}$ curves for the leading-edge and trailing-edge cases are noticeably different from the corresponding $\mathcal{L}^{ref}$ curves. However, whether or not there is a substantial difference between $\mathcal{L}^{net}$ and $\mathcal{L}^{ref}$ for LEV initiation for any particular pivot location depends on the value of U_{net}/U_{ref} at event I. Because event I occurs at a low pitch angle of 15 degrees for the leading-edge case, U_{net}/U_{ref} is close to 1, at 1.08, and there is little difference between $\mathcal{L}^{net}$ and $\mathcal{L}^{ref}$ for event I for this pivot location. On the other hand, for the TE pivot, event I occurs at a large pitch angle of 58 degrees at which U_{net}/U_{ref} is 0.7. This deviation of U_{net}/U_{ref} from the value of 1 results in a larger difference between $\mathcal{L}^{net}$ and $\mathcal{L}^{ref}$ for event I for this case. In general, except for the high-K, aft-pivot cases which form the outliers in figure 19, event I for the low-Re cases occurs at low pitch angles at which U_{net}/U_{ref} is close to 1, resulting in only small differences between $\mathcal{L}^{net}$ and $\mathcal{L}^{ref}$ for LEV initiation.

For the high-Re condition, examining the results for the medium-K cases in figure 38(a), we see similarity with the low-Re, medium-K results. Because $U_{net}/U_{ref}(t)$, which is independent of Re, does not deviate much from the value of 1 at any time during the motion, there is no noticeable difference between the time variations of the $\mathcal{L}^{ref}$ and the $\mathcal{L}^{net}$ curves. However, the values of $\mathcal{L}$ for event I for all three pivot cases for the high-Re, medium-K cases are higher than those for the corresponding low-Re, medium-K cases. As already mentioned in § 5.2, this difference can be attributed to the delayed boundary-layer separation at the higher Reynolds numbers due to the energizing effects of modelled turbulence.

The most significant effect of the updated LESP formulation is seen at the high-Re and high-K conditions. Examining the results in figure 38(b), it is seen that event I occurs

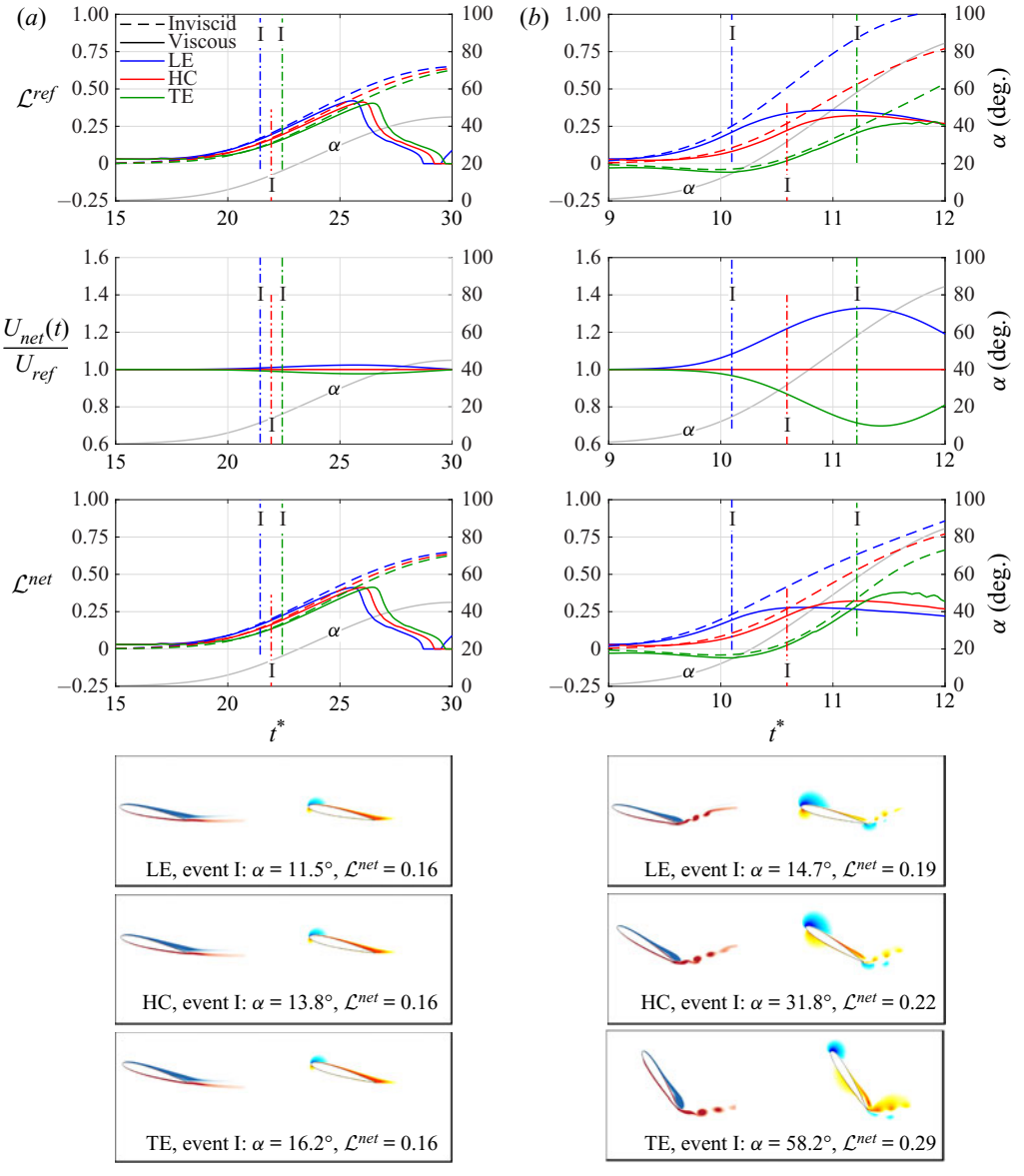

FIGURE 37. Plots of $\mathcal{L}$ and U_{net}/U_{ref} vs t^* variations, and flow contours for the NACA 0012 aerofoil at $Re = 30\,000$ for three pivot locations for (*a*) $K = 0.05$ and (*b*) $K = 0.40$.

at high pitch angles of between 43 and 76 degrees. As a result, the values for U_{net}/U_{ref} for event I for the LE and TE pivot cases (which are 1.3 and 0.75, respectively) deviate substantially from the value of 1, and result in substantial differences between the $\mathcal{L}^{ref}$ and the $\mathcal{L}^{net}$ for event I for the non-half-chord pivot locations. It is as a result of this velocity scaling that the large scatter in $\mathcal{L}^{ref}$ for event I for different pivot locations seen in figure 16 is substantially removed in figure 20 when the updated formulation with $\mathcal{L}^{net}$ is used.

Finally, it is also interesting to note that the $\mathcal{L}^{net}(t)$ curves for the three high-K pivot cases (at either Reynolds number) all have maximum values that are close to each other.

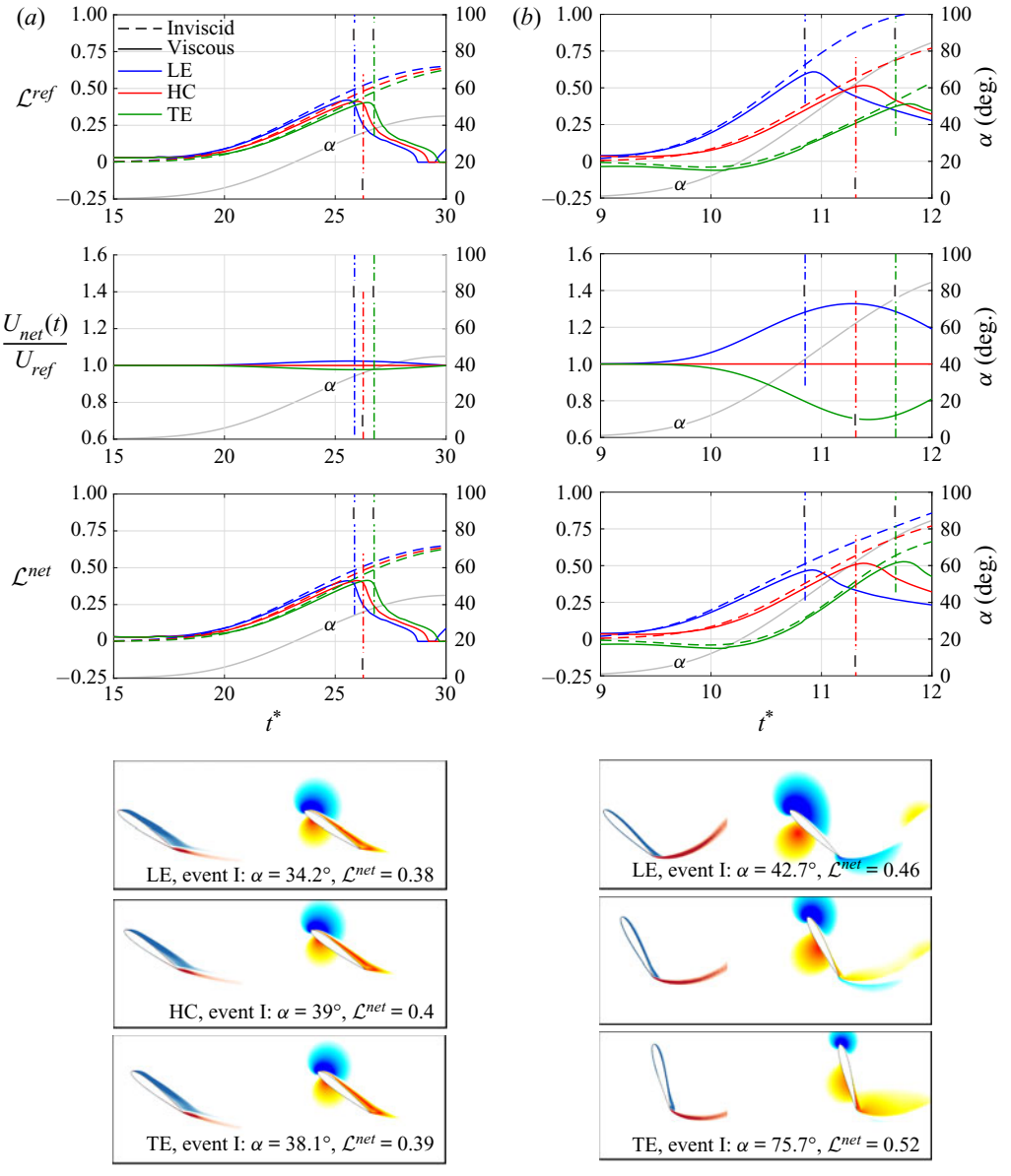

FIGURE 38. Plots of $\mathcal{L}$ and U_{net}/U_{ref} vs t^* variations, and flow contours for the NACA 0012 aerofoil at $Re = 3$ million for three pivot locations for (*a*) $K = 0.05$ and (*b*) $K = 0.40$.

This behaviour is not seen with the $\mathcal{L}^{ref}(t)$ curves. This result shows that the $\mathcal{L}^{net}(t)$ better captures the maximum possible suction that the aerofoil leading edge can support at a given Reynolds number even between different motion cases.

REFERENCES

AKBARI, M. H. & PRICE, S. J. 2003 Simulation of dynamic stall for a NACA0012 airfoil using a vortex method. *J. Fluids Struct.* **17**, 855–874.

ANSELL, P. J. & MULLENERS, K. 2020 Multiscale vortex characteristics of dynamic stall from empirical mode decomposition. *AIAA J.* **58** (2), 600–617.

BEDDOES, T. S. 1978 Onset of leading-edge separation effects under dynamic conditions and low Mach number. In *Proceedings of the 34th Annual National Forum of the American Helicopter Society*.

CARR, L. W., MCALISTER, K. W. & MCCROSKEY, W. J. 1977 Analysis of the development of dynamic stall based on oscillating airfoil experiments. *NASA Tech. Rep.* TN 8382. National Aeronautics and Space Administration.

CARR, L. W., MCCROSKEY, W. J., MCALISTER, K. W., PUCCI, S. L. & LAMBERT, O. 1982 An experimental study of dynamic stall on advanced airfoil sections. Volume 3: hot-wire and hot-film measurements. *NASA Tech. Rep.* TM 84245. National Aeronautics and Space Administration.

CARTA, F. 1967*a* An analysis of the stall flutter instability of helicopter rotor blades. *J. Am. Helicopter Soc.* **12**, 1–18.

CARTA, F. 1967*b* Unsteady normal force on an airfoil in a periodically stalled inlet flow. *J. Aircraft* **4** (5), 416–442.

CASSIDY, D. A., EDWARDS, J. R. & TIAN, M. 2009 An investigation of interface-sharpening schemes for multiphase mixture flows. *J. Comput. Phys.* **228** (16), 5628–5649.

CHANDRASEKHARA, M. S., AHMED, S. & CARR, L. W. 1993 Schlieren studies of compressibility effects on dynamic stall of transiently pitching airfoils. *J. Aircraft* **30** (2), 213–220.

CHOUDHURI, P. G. & KNIGHT, D. D. 1996 Effects of compressibility, pitch rate, and Reynolds number on unsteady incipient leading-edge boundary layer separation over a pitching airfoil. *J. Fluid Mech.* **308**, 195–217.

CHOUDHURI, P. G., KNIGHT, D. D. & VISBAL, M. R. 1994 Two-dimensional unsteady leading-edge separation on a pitching airfoil. *AIAA J.* **32** (4), 673–681.

CORKE, T. C. & THOMAS, F. O. 2015 Dynamic stall in pitching airfoils: aerodynamic damping and compressibility effects. *Annu. Rev. Fluid Mech.* **47**, 479–505.

CRIMI, P. 1973 Dynamic stall. *Tech. Rep.* AGARD-AG 172.

DAT, R., TRAN, C. T. & PETOT, D. 1979 Modele Phenomenologique de Decrochage Dynamique sur Profil de Pale d'Helicoptere. *ONERA Tech. Rep.* TP 1979-149.

DEPARDAY, J. & MULLENERS, K. 2019 Modeling the interplay between the shear layer and leading edge suction during dynamic stall. *Phys. Fluids* **31** (10), 107104.

EDWARDS, J. R. & CHANDRA, S. 1996 Comparison of eddy viscosity – transport turbulence models for three-dimensional, shock-separated flowfields. *AIAA J.* **34** (4), 756–763.

EKATERINARIS, J. A. & PLATZER, M. F. 1998 Computational prediction of airfoil dynamic stall. *Prog. Aerosp. Sci.* **33** (11–12), 759–846.

ELDREDGE, J. D. & JONES, A. R. 2019 Leading-edge vortices: mechanics and modeling. *Annu. Rev. Fluid Mech.* **51**, 75–104.

ELDREDGE, J. D. & WANG, C. 2010 High-fidelity simulations and low-order modeling of a rapidly pitching plate. *AIAA Paper* 2010-4281. American Institute of Aeronautics and Astronautics.

ELDREDGE, J. D. & WANG, C. 2011 Improved low-order modeling of a pitching and perching plate. *AIAA Paper* 2011-3579. American Institute of Aeronautics and Astronautics.

ELDREDGE, J. D., WANG, C. J. & OL, M. V. 2009 A computational study of a canonical pitch-up, pitch-down wing maneuver. *AIAA Paper* 2009-3687. American Institute of Aeronautics and Astronautics.

ELLINGTON, C. 1999 The novel aerodynamics of insect flight: applications to micro-air vehicles. *J. Expl Biol.* **202** (23), 3439–3448.

ELLINGTON, C. P., VAN DEN BERG, C., WILLMOTT, A. P. & THOMAS, A. L. R. 1996 Leading-edge vortices in insect flight. *Nature* **384**, 626–630.

EPPS, B. P. & GREELEY, D. S. 2018 A quasi-continuous vortex lattice method for unsteady aerodynamics analysis. *AIAA Paper* 2018-0815. American Institute of Aeronautics and Astronautics.

EPPS, B. P. & ROESLER, B. T. 2018 Vortex sheet strength in the Sears, Küssner, Theodorsen, and Wagner aerodynamics problems. *AIAA J.* **56** (3), 889–904.

ERICSSON, L. E. & REDING, J. P. 1971 Unsteady airfoil stall, review and extension. *J. Aircraft* **8** (8), 609–616.

EVANS, W. T. & MORT, K. W. 1959 Analysis of computed flow parameters for a set of sudden stalls in low speed two-dimensional flow. *NACA Tech. Rep.* TN D-85.

GEISSLER, W. & HASELMEYER, H. 2006 Investigation of dynamic stall onset. *Aerosp. Sci. Technol.* **10**, 590–600.

GORMONT, R. E. 1973 A mathematical model of unsteady aerodynamics and radial flow for application to helicopter rotors. Army Air Mobility Research and Develpment Laboratory TR 767240.

GRANLUND, K., OL, M. V. & BERNAL, L. 2011 Experiments on pitching plates: force and flowfield measurements at low Reynolds numbers. *AIAA Paper* 2011-0872. American Institute of Aeronautics and Astronautics.

GRANLUND, K., OL, M. V., GARMANN, D. J., VISBAL, M. R. & BERNAL, L. 2010 Experiments and computations on abstractions of perching. *AIAA Paper* 2010-4943. American Institute of Aeronautics and Astronautics.

GUPTA, R. & ANSELL, P. J. 2019 Unsteady flow physics of airfoil dynamic stall. *AIAA J.* **57** (1), 165–175.

GURSUL, I. 2005 Review of unsteady vortex flows over slender delta wings. *J. Aircraft* **42** (2), 299–319.

HILL, J. L., SHAW, S. T. & QIN, N. 2004 Investigation of transition modelling for a aerofoil dynamic stall. In *Proceedings of the 24th International Congress of Aeronautical Sciences, Yokohama, Japan*.

HIRATO, Y., SHEN, M., GOPALARATHNAM, A. & EDWARDS, J. R. 2019 Vortex-sheet representation of leading-edge vortex shedding from finite wings. *J. Aircraft* **56** (4), 1626–1640.

HOU, W., DARAKANANDA, D. & ELDREDGE, J. D. 2019 Machine-learning-based detection of aerodynamic disturbances using surface pressure measurements. *AIAA J.* **57** (12), 5079–5093.

HUYER, S. A., SIMMS, D. & ROBINSON, M. C. 1996 Unsteady aerodynamics associated with a horizontal-axis wind turbine. *AIAA J.* **34** (7), 1410–1419.

JONES, K. & PLATZER, M. 1998 On the prediction of dynamic stall onset on airfoils in low speed flow. In *Proceedings of the 8th International Symposium on Unsteady Aerodynamics and Aeroelasticity of Turbomachines*, pp. 797–812. Kluwer.

KATZ, J. 1981 Discrete vortex method for the non-steady separated flow over an airfoil. *J. Fluid Mech.* **102**, 315–328.

KATZ, J. & PLOTKIN, A. 2000 *Low-Speed Aerodynamics*. Cambridge Aerospace Series. Cambridge University Press.

KATZ, J. & PLOTKIN, A. 2001 *Low-Speed Aerodynamics*, 2nd edn. Cambridge University Press.

LARSEN, J. W., NIELSEN, S. R. K. & KRENK, S. 2007 Dynamic stall model for wind turbine airfoils. *J. Fluids Struct.* **23** (7), 959–982.

LEISHMAN, J. G. 1990 Dynamic stall experiments on the NACA 23012 aerofoil. *Exp. Fluids* **9**, 49–58.

LEISHMAN, J. G. 2002 *Principles of Helicopter Aerodynamics*, Cambridge Aerospace Series. Cambridge University Press.

LEISHMAN, J. & BEDDOES, T. 1989 A semi-empirical model for dynamic stall. *J. Am. Helicopter Soc.* **34** (3), 3–17.

LIU, Z., LAI, J. C., YOUNG, J. & TIAN, F.-B. 2016 Discrete vortex method with flow separation corrections for flapping-foil power generators. *AIAA J.* **55** (2), 410–418.

MCALISTER, K. W. & CARR, L. W. 1978 Water-tunnel experiments on an oscillating airfoil at $Re = 21{,}000$. *NASA Tech. Rep.* TM 78446. National Aeronautics and Space Administration.

MCALISTER, K. W., CARR, L. W. & MCCROSKEY, W. J. 1978 Dynamic stall experiments on the NACA0012 airfoil. *NASA Tech. Rep.* TP 1100. National Aeronautics and Space Administration.

MCALISTER, K. W., PUCCI, S. L., MCCROSKEY, W. J. & CARR, L. W. 1982 An experimental study of dynamic stall on advanced airfoil sections. Volume 2: pressure and force data. *NASA Tech. Rep.* TM 84245. National Aeronautics and Space Administration.

MCCROSKEY, W. 1982 Unsteady airfoils. *Annu. Rev. Fluid Mech.* **14**, 285–311.

MCCROSKEY, W. J. 1981 The phenomenon of dynamic stall. *NASA Tech. Rep.* TM 81264. National Aeronautics and Space Administration.

MCCROSKEY, W. J., CARR, L. W. & MCALISTER, K. W. 1976 Dynamic stall experiments on oscillating airfoils. *AIAA J.* **14** (1), 57–63.

MCCROSKEY, W. J., MCALISTER, K. W., CARR, L. W. & PUCCI, S. L. 1982 An experimental study of dynamic stall on advanced airfoil sections. Volume 1: summary of the experiment. *NASA Tech. Rep.* TM 84245. National Aeronautics and Space Administration.

MORRIS, W. J. & RUSAK, Z. 2013 Stall onset on aerofoils a low to moderately high Reynolds number flows. *J. Fluid Mech.* **733**, 439–472.

MULLENERS, K. & RAFFEL, M. 2012 The onset of dynamic stall revisited. *Exp. Fluids* **52**, 779–793.

NARSIPUR, S. 2017 Low-order modeling of dynamic stall on airfoils in incompressible flow. PhD thesis, North Carolina State University, Raleigh, NC.

NARSIPUR, S., GOPALARATHNAM, A. & EDWARDS, J. R. 2018 Low-order modeling of airfoils with massively separated flow and leading-edge vortex shedding. In *Proceedings of the AIAA Aerospace Science Meeting, Kissimmee, FL*, 2018-0813.

NARSIPUR, S., GOPALARATHNAM, A. & EDWARDS, J. R. 2019 Low-order model for prediction of trailing-edge separation in unsteady flow. *AIAA J.* **57** (1), 191–207.

OL, M., BERNAL, L., KANG, C. & SHYY, W. 2009 Shallow and deep dynamic stall for flapping low Reynolds number airfoils. *Exp. Fluids* **46** (5), 883–901.

PETERS, D. A., KARUNAMOORTHY, S. & CAO, W.-M. 1995 Finite state induced flow models. I – two-dimensional thin airfoil. *J. Aircraft* **32** (2), 313–322.

RAMESH, K. 2020 On the leading-edge suction and stagnation-point location in unsteady flows past thin aerofoils. *J. Fluid Mech.* **886**, A13.

RAMESH, K., GOPALARATHNAM, A., EDWARDS, J. R., OL, M. V. & GRANLUND, K. 2013 An unsteady airfoil theory applied to pitching motions validated against experiment and computation. *J. Theor. Comput. Fluid Dyn.* **27** (6), 843–864.

RAMESH, K., GOPALARATHNAM, A., GRANLUND, K., OL, M. V. & EDWARDS, J. R. 2014 Discrete-vortex method with novel shedding criterion for unsteady airfoil flows with intermittent leading-edge vortex shedding. *J. Fluid Mech.* **751**, 500–538.

RAMESH, K., GRANLUND, K., OL, M. V., GOPALARATHNAM, A. & EDWARDS, J. R. 2017 Leading-edge flow criticality as a governing factor in leading-edge vortex initiation in unsteady airfoil flows. *J. Theor. Comput. Fluid Dyn.* **32** (2), 109–136.

RAMESH, K., MURUA, J. & GOPALARATHNAM, A. 2015 Limit-cycle oscillations in unsteady flows dominated by intermittent leading-edge vortex shedding. *J. Fluids Struct.* **55**, 84–105.

RAMSAY, R. R., GREGOREK, G. M. & HOFFMANN, M. J. 1996 Effects of grit roughness and pitch oscillations on the S801 airfoil. National Renewable Energy Laboratory Report NREL/TP-442-7818.

SELIG, M. S., DONOVAN, J. F. & FRASER, D. B. 1989 *Airfoils at Low Speeds*. Soartech 8, SoarTech Publications.

SHARMA, A. & VISBAL, M. 2019 Numerical investigation of the effect of airfoil thickness on onset of dynamic stall. *J. Fluid Mech.* **870**, 870–900.

SHENG, W., GALBRAITH, R. A. M. & COTON, F. N. 2006 A new stall-onset criterion for low speed dynamic-stall. *J. Solar Energy Engng* **128** (4), 461–471.

SHENG, W., GALBRAITH, R. A. M. & COTON, F. N. 2008 A modified dynamic stall model for low Mach numbers. *J. Solar Energy Engng* **130** (3), 31013–31023.

SPALART, P. R. & ALLMARAS, S. R. 1992 A one-equation turbulence model for aerodynamic flows. *AIAA Paper* 92-0439. American Institute of Aeronautics and Astronautics.

SPENTZOS, A., BARAKOS, G., BADCOCK, K., RICHARDS, B., WERNERT, P., SCHRECK, S. & RAFFEL, M. 2004 CFD investigation of 2D and 3D dynamic stall. In *Proceedings of the AHS 4the Decennial Specialist's Conference on Aeromechanics, San Francisco, California, USA*. American Helicopter Society International.

TAHA, H. & REZAEI, A. S. 2019 Viscous extension of potential-flow unsteady aerodynamics: the lift frequency response problem. *J. Fluid Mech.* **868**, 141–175.

THEODORSEN, T. 1935 General theory of aerodynamic instability and the mechanism of flutter. *NACA Tech. Rep.* 496.

VISBAL, M. R. & GARMANN, D. J. 2019 Dynamic stall of a finite-aspect-ratio wing. *AIAA J.* **57** (3), 962–977.

VISBAL, M. R. & SHANG, J. S. 1989 Investigation of the flow structure around a rapidly pitching airfoil. *AIAA J.* **27** (8), 1044–1051.

WAGNER, H. 1925 Über die Entstehung des dynamischen Auftriebes von Tragflügeln. *Z. Angew. Math. Mech.* **5** (1), 17–35.

WANG, C. & ELDREDGE, J. 2013 Low-order phenomenological modeling of leading-edge vortex formation. *J.Theor. Comput. Fluid Dyn.* **27** (5), 577–598.

WERNERT, P., GEISSLER, W., RAFFEL, M. & KOMPENHAUS, J. 1996 Experimental and numerical investigations of dynamic stall on a pitching airfoil. *AIAA J.* **34** (5), 982–989.

XIA, X. & MOHSENI, K. 2017 Unsteady aerodynamics and vortex-sheet formation of a two-dimensional airfoil. *J. Fluid Mech.* **830**, 439–478.

YAN, Z., TAHA, H. E. & HAJJ, M. R. 2014 Geometrically-exact unsteady model for airfoils undergoing large amplitude maneuvers. *Aerosp. Sci. Technol.* **39**, 293–306.

YOUNG, J., LAI, J. C. S. & PLATZER, M. F. 2014 A review of progress and challenges in flapping foil power generation. *Prog. Aerosp. Sci.* **67**, 2–28.